Perturbation-induced seeding and crystallization of hybrid perovskites over surface-modified substrates for optoelectronic devices

Ahmad, Riyas; Surendran, Abhijith; Harikesh, Padinhare Cholakkal; Haselsberger, Reinhard; Nur Fadilah Jamaludin; John, Rohit Abraham; Koh, Teck Ming; Bruno, Annalisa; Leong, Wei Lin; Mathews, Nripan; Michel-Beyerle, Maria-Elisabeth; Mhaisalkar, Subodh Gautam

2019

Ahmad, R., Surendran, A., Harikesh, P. C., Haselsberger, R., Nur Fadilah Jamaludin, John, R. A., . . . Mhaisalkar, S. G. (2019). Perturbation-induced seeding and crystallization of hybrid perovskites over surface-modified substrates for optoelectronic devices. ACS Applied Materials & Interfaces, 11(31), 27727-27734. doi:10.1021/acsami.9b05965

https://hdl.handle.net/10356/142577

https://doi.org/10.1021/acsami.9b05965

Perturbation Induced Seeding and Crystallization of Hybrid Perovskites Over Surface Modified Substrates for Optoelectronic Devices

Riyas Ahmad[a,b,c], Abhijith Surendran[e], P. C. Harikesh[a,b,d], Haselsberger Reinhard[c], Nur Fadilah Jamaludin[a,b,d], Rohit Abraham John[d], Teck Ming Koh[a], Annalisa Bruno[a], Wei Lin Leong[e,f], Nripan Mathews[a,d], Maria-Elisabeth Michel-Beyerle[c] and Subodh G. Mhaisalkar[a,d]*

a. Energy Research Institute at NTU (ERI@N), Research Techno Plaza, X-Frontier Block Level 5, 50 Nanyang Drive, Singapore 637553.
b. Interdisciplinary Graduate School (IGS), Nanyang Technological University, 50 Nanyang Avenue, Singapore 639798.
c. Division of Physics and Applied Physics, School of Physical and Mathematical Sciences (SPMS), Nanyang Technological University, 21 Nanyang Link, Singapore 637371.
d. School of Materials Science and Engineering, Nanyang Technological University, 50 Nanyang Avenue, Singapore 639798.
e. School of Electrical and Electronic Engineering, Nanyang Technological University, 50 Nanyang Avenue, Singapore 639798.
f. School of Chemical and Biomedical Engineering, Nanyang Technological University, 70 Nanyang Drive, Singapore 637459.

Corresponding Author

* Prof. Nripan Mathews (Email: Nripan@ntu.edu.sg)

Keywords: Lead halide perovskites, crystal growth, photodetectors, precursor colloids, anti-solvent vapour crystallization.

ABSTRACT

Growing a monocrystalline layer of lead halide perovskites directly over substrates is necessary to completely harness its stellar properties in optoelectronic devices as the single crystals of these materials are extremely brittle. We study the crystallization mechanism of perovskites by anti-solvent vapor diffusion to its precursor solution and find that heterogeneous nucleation prevails in the process, with the crystallization dish walls providing the energy to overcome the nucleation barrier. By perturbing the system using sonication we are able to introduce homogenously nucleated seed crystals in the precursor solution. These seeds lead to the growth of closely packed crystals over surface modified substrates kept in the precursor solution. This crystallization process is substrate independent and scalable, can be utilized to fabricate planar optoelectronic devices. We fabricate planar photoconductors with these crystal film which reports a colossal detectivity (1.48×10^{13} Jones) for methylammonium lead iodide crystal photoconductors.

TOC GRAPHICS

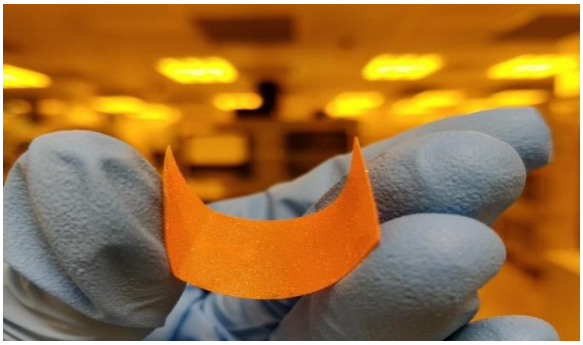

INTRODUCTION

With intriguing electronic and optoelectronic properties such as long carrier diffusion lengths, high carrier lifetimes and extremely low trap densities arising from its inherent defect tolerance,[1] hybrid lead halide perovskites have revolutionized the field of photovoltaics,[2] light emitting diodes(LEDs)[3] and other optoelectronic devices.[4–7] Almost all these devices use a spin coated polycrystalline thin film of hybrid lead halide perovskites (hereafter referred to as perovskites). In these normal polycrystalline thin films, all the alluring attributes inherent to the material are not harnessed and are immensely compromised. For instance, a good quality polycrystalline thin film of perovskites (methyl ammonium lead bromide/iodide) has a trap density of the order of 10^{17} cm^{-3}.[8] Because of these traps, the diffusion length and lifetime of the charge carriers in the polycrystalline thin films get dwindled drastically.

In contrast, for perovskite single crystals, the reported trap state densities are of the order of 10^{9} to 10^{10} cm^{-3}, which is extremely low and comparable to the best quality ultra-pure single crystalline silicon.[9] In single crystals, the electron and hole diffusion lengths were found to be of the order of hundreds of microns.[10,11] The limited trap density also results in long photo-generated carrier lifetimes (above 1μs) even for facile solution grown crystals.[9] While it has been found that, the majority of the losses in a photovoltaic cell are caused by dangling bonds at the interfaces,[12] bulk traps are responsible for limiting the device performances to an extent. Apart from the reduction in carrier mobility as well as diffusion length and the resultant deterioration of the device performances and efficiency, the grain boundaries in thin films act as active centers for moisture diffusion, thereby deteriorating its moisture tolerance.[13] Grain boundaries also act as a channel for ionic migration, which results in ionic accumulation at the device interfaces and causes anomalous

device characteristics.[14–16] In short, improvement in crystallinity not only improves the device performance but also endows coherent device characteristics and long-term stability. Thus, like most of the other optoelectronic technologies, a monocrystalline perovskite device is expected to show superior performances, improved stability and reliability.

The most common method to fabricate monocrystalline optoelectronic devices is to grow a large bulk single crystal of the optoelectronic material which is later sliced down to thin wafers for the device fabrication. Another method relies on growing thin monocrystalline layers of the material epitaxially over the device substrates. For perovskites it is extremely difficult to slice down the crystals to thin wafers owing to its inherent brittleness and fragility.[17,18] Therefore, a viable option to realize an efficient and stable perovskite device is to grow its monocrystalline layer over the substrates[19]. Even though fast, simple and efficient growth of free standing single crystals of hybrid perovskites have been achieved, [9,11] their monocrystalline growth on substrates above a few centimeters in dimensions, as well as growing compact perovskite films with submillimeter grain sizes still remain a challenge and provides an avenue for the future research.

In this work, we examined the mechanism of anti-solvent vapor crystallization (AVC) where a bad solvent vapor is allowed to diffuse to the perovskite precursor solution to cause supersaturation and crystallization (the case of thin film spin coating with anti-solvent dripping is similar to this as well).[9] Even though growth of methylammonium lead bromide ($MAPbBr_3$) crystals over substrates have been demonstrated, methylammonium lead iodide ($MAPbI_3$) crystal growth over substrates are difficult to realize due to intrinsic anisotropic growth of tetragonal crystals.[20,21] To the best of our knowledge this is the first work investigating the mechanism of AVC in perovskites. We found that crystal growth in AVC can be modified by varying the surface energy of the

crystallization dish. Our investigation of the process enabled us to modify and optimize it to grow densely packed crystals (crystal sizes > 100 µm) of methylammonium lead iodide ($MAPbI_3$) as well as methylammonium lead bromide ($MAPbBr_3$) over substrates. We used ultrasonication to create nucleation and growth of perovskite crystals in the precursor (sonication modified anti-solvent vapor crystallization – S-AVC). Since the initial nucleation and seed crystal growth for S-AVC took place in precursor solution, it enabled the growth perovskite crystals over any substrates and can be used as a universal technique for the fabrication of planar optoelectronic devices (Figure 1). These densely packed, highly crystalline film were used to fabricate photodetectors having a very high detectivity of 1.48 x 10^{13} Jones and a high responsivity of 20 AW^{-1} for a 445 nm illumination.

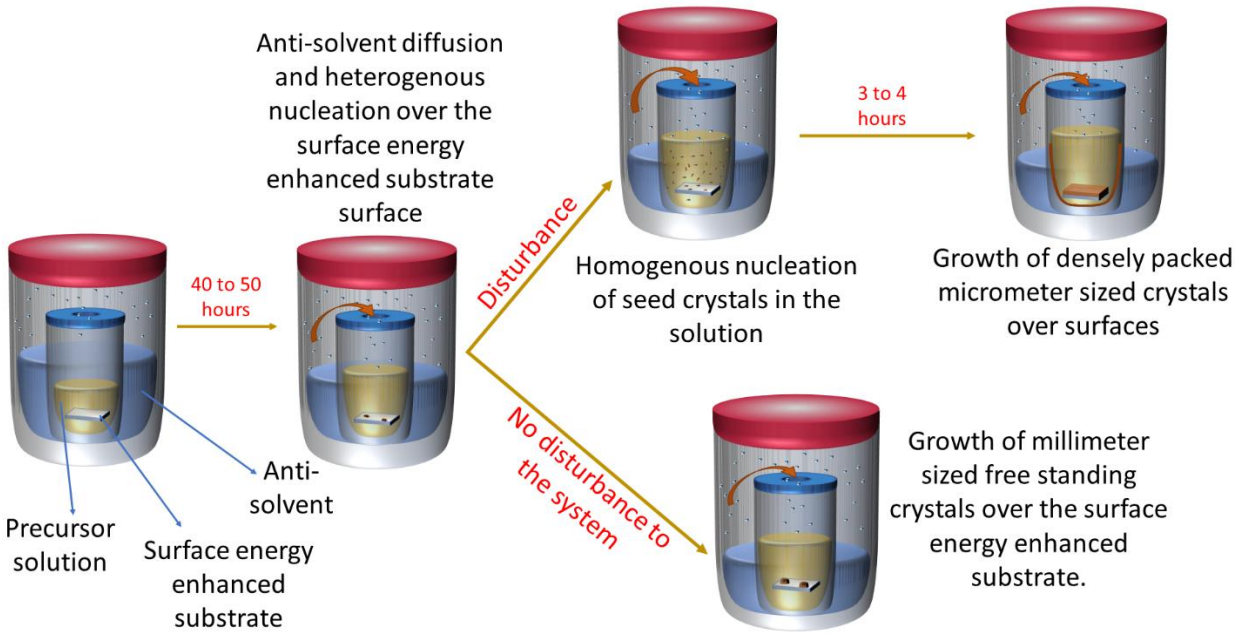

Figure 1. Schematic showing the crystallization procedure in AVC and sonication modified AVC. The sonication creates homogenously nucleated seeds, which grow over the substrate kept in the crystallization dish.

EXPERIMENTAL SECTION

Precursor Solution Preparation and AVC: Lead iodide (PbI_2) and methylammonium iodide (MAI) were stoichiometrically dissolved in γ-butyrolactone (GBL), lead bromide ($PbBr_2$) and methylammonium bromide (MABr) were dissolved in dimethylformamide (DMF) to create the precursor solutions. These precursor solutions were used to perform dynamic light scattering measurements as well.

Dichloromethane (DCM) was used as anti-solvent. As shown in figure 1, the crystallization dish is kept inside a container with DCM. The anti-solvent evaporates and move to the inner crystallization dish resulting in crystallization of bulk perovskite crystals. (see supporting information for detailed crystallization procedure). The sonication modified AVC was used to grow crystals over substrates.

S-AVC and Photodetector Fabrication: As the anti-solvent introduction create supersaturation and the crystals start forming inside the precursor, a short duration of sonication induces the formation of numerous homogenously nucleated seed crystals in the precursor, which then get attached substrates kept inside the precursor. As more and more anti-solvent gets transferred inside, these seed crystals grow over the substrates and forms a pin hole free thick crystal film over substrates.

For the fabrication of photodetector, we kept laser etched interdigitated FTO electrodes patterned over glass substrate. The perovskite crystals grow over these substrates to form FTO/perovskite/FTO photoconductors. A detailed fabrication and measurement procedure is provided in the supporting information.

RESULTS AND DISCUSSION

Mechanism of anti-solvent vapor crystallization in lead halide perovskites: The basic mechanism of AVC was investigated for both $MAPbI_3$ and $MAPbBr_3$. Light scattering was observed if we shine a 650 nm laser beam through the precursor solution. Both the precursors showed significant light scattering as a result of its colloidal nature, with the particle size of the order of hundreds of nm (Figure S1, Figure S2). These results were well in accordance to the previous reports regarding the behavior of perovskite precursors. The solvent molecules formed coordination complexes with lead halides in the dispersion and resulted in the formation of large colloidal particles which are stabilized by the presence of other organic ions in the system.[22,23] The anti-solvent vapor was allowed to slowly diffuse to these precursor dispersions to facilitate crystallization. In conventional anti-solvent crystallization methods (for example: NaCl, Na_2CO_3 crystals), anti-solvent introduction drives out the dissolving solvents and thereby creates supersaturation and crystal growth in the precursor which is associated with an increase in the colloidal particle size.[24–26] In contrast, perovskite precursors showed a reduced tyndall effect after millimeter sized crystals were grown out of them. This shows a reduction in the particle size of the precursors and this reduction in the particle size is due to the consumption of precursors from the dispersion while crystallization (Figure S1, S2). To get a deeper insight over the crystallization procedure, UV-Visible absorption spectroscopy was carried out for the precursor dispersion before, during as well as after anti-solvent introduction and crystallization (Figure S3). The spectrum before anti-solvent introduction showed sharp absorption edges at 490 nm and at 400 nm for $MAPbI_3$ and $MAPbBr_3$ respectively. The absorption edges were blue shifted upon anti-solvent introduction. As anti-solvents were introduced and caused crystallization by consuming the precursors from the ‘dispersion’ bulk, it resulted in the dilution of the precursor. As the

concentration was decreased, the ratio of metal halide to ligand varied, causing the formation of smaller coordination complexes which appeared as the blue shifted absorption edge[22,23]. This was verified by observing the absorption edge of a 1000x diluted precursor using the same solvents (DMF and GBL for $MAPbBr_3$ and $MAPbI_3$ respectively). It was found that the absorption edge was further blue shifted upon dilution. Surprisingly, the precursor dispersion during and after anti-solvent introduction didn't show any $MAPbBr_3$ or $MAPbI_3$ perovskite crystal absorption peaks, not even after crystals of millimeter sizes were formed out of them. At the precursor concentrations used, we observed that the perovskite crystals were always forming over the walls of the crystallization dish and the precursor remained transparent throughout the crystallization procedure. To confirm that no colloidal perovskite nanocrystals were formed in the precursor, it was illuminated with UV at different stages of anti-solvent evaporation. The precursor didn't show any photoluminescence at normal perovskite emission regimes (Figure S4 and S5).

Summarizing all these results and observations, we deduced that the crystallization happened exclusively on the surfaces of the crystallization dish (heterogeneous nucleation and growth) and not at the bulk of precursor dispersion. The energy to overcome the nucleation barrier is provided by the crystallization dish surface, and the crystals kept on growing over the surfaces by consuming the precursors surrounding the nuclei. As more precursors were consumed for the crystal growth, the coordination chemistry changed and the sizes of the particles in the colloid were reduced, which is evident from the reduced tyndall effect (Figure 2a, detailed explanation in supporting information). The formation of large and stable coordination complexes in the precursor might be the reason for this distinct kind of crystallization for hybrid perovskites. To confirm our hypothesis regarding the effect of surface energy of the crystallization dish over the crystallization process, we carried out AVC with surface modified crystallization dishes.

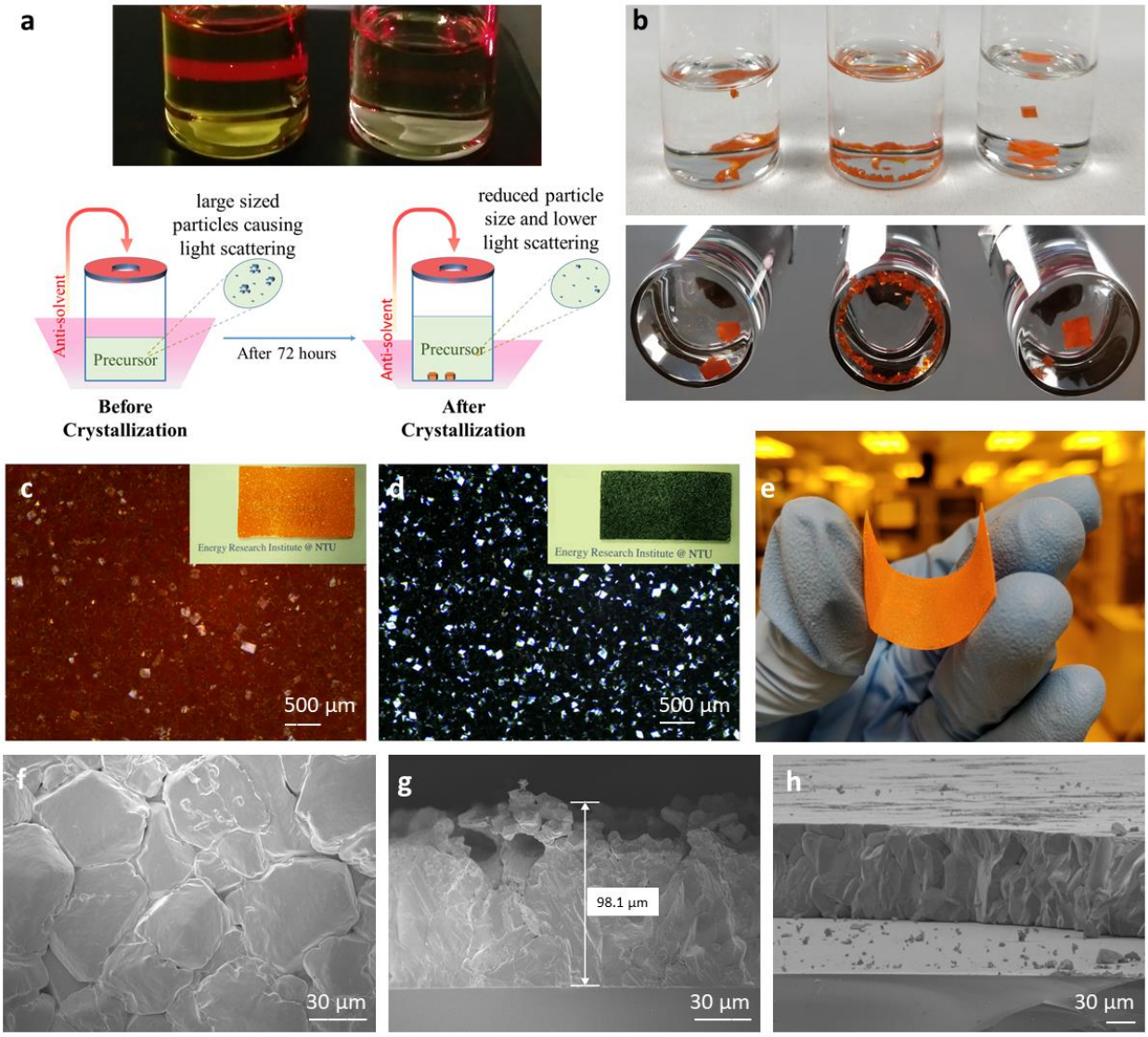

Figure 2. a) Light scattering from the precursor before and after crystallization. b) Optical image of crystallization in surface energy modified dishes: bare glass dish (left), surface energy reduced dish by OTS (middle), surface energy increased by APTMS (right) and their corresponding bottom views. c) and d) Optical and 50x magnified images of $MAPbBr_3$ and $MAPbI_3$ crystals respectively grown over glass (1.5cm x 2.5cm) by S-AVC. e) $MAPbBr_3$ crystals grown over flexible polyethylene terephthalate coated with indium doped tin oxide. f) and g) SEM images of $MAPbI_3$

crystals grown over glass and its cross section. h) $MAPbI_3$ crystals grown over glass and polished by optical sandpaper.

The surfaces of the crystallization dishes were coated with self-assembled monolayers (SAM) of hydrophobic octadecyltrichlorosilane (OTS) and hydrophilic aminopropyltrimethoxysilane (APTMS) to respectively reduce and increase the surface energy.[27–30] The crystals grown in dishes with increased surface energy had large facet area parallel to the walls of crystallization dishes and crystals started forming over both horizontal and vertical walls of the dish. However, in the case of reduced surface energy, no crystals were found over the vertical or horizontal walls of the dish. Instead, numerous tiny crystals started crystallizing out at the corners formed by the intersection of horizontal and vertical walls of the crystallizing dish, where the surface energy could be predominantly high (Figure 2b). All these results vindicate our assumption that the surface energy of the crystallization dish provided the energy enough to overcome the nucleation barrier in AVC.

The sonication modified AVC: In our sonication modulated crystal growth technique, the walls of the crystallization dish were coated with hydrophobic SAM (OTS) and the substrate over which crystals need to be grown were coated with hydrophilic SAM (APTMS). A short duration (1s) ultrasound was used to disturb the AVC system to create the growth of $MAPbBr_3$ as well as $MAPbI_3$ crystals over any substrates (S-AVC). Upon perturbation of the supersaturated precursor, the color of the precursor dispersion turned slightly from colorless to orange in $MAPbBr_3$ (from yellow to grey in $MAPbI_3$) indicating that the nucleation and growth of seed crystals were initiated in the dispersion. This showed that the normal AVC, where heterogeneous nucleation prevailed

was altered upon perturbation and resulted in homogeneous nucleation and crystal growth in the precursor dispersion. As the seed crystals started growing in the precursor dispersion, they got attached to the walls of crystallization dish and the substrate kept inside it to attain stability, as explained by the schematic Figure 1. Further anti-solvent introduction to the precursor resulted in the growth of these seed crystals over the substrates. This led to the formation of densely packed, highly crystalline $MAPbBr_3$ and $MAPbI_3$ layers with an area of a few square centimeters over rigid as well as flexible substrates, as shown in Figure 2c, 2d and 2e. The typical thickness of the $MAPbI_3$ film was of the order of 100μm after 3 hours of growth and was pinhole free (Figure 2f and 2g) (Figure S6 for $MAPbBr_3$ crystal film). As the substrates were coated with $-NH_3$ terminated and hydrophilic (APTMS) SAM, it helped the crystals for a close packed growth over the substrates and gave strong adhesiveness between them. It was possible to mechanically polish the crystals grown over glass with optical sandpapers owing to their good substrate adhesiveness (Figure 2h and Figure S7). Since the nucleation and initial crystal growth took place in the precursor, the crystal growth was independent of substrate surfaces (Figure S8, S9), and the crystal films were able to sustain high tensile forces making it easy to process them and fabricate into devices (Figure S10). Thus, S-AVC deposition can be used as a universal method to grow hybrid perovskite crystals over any substrates.

The crystallinity and orientation of the crystal film was investigated using X-ray diffraction (Figure 3a and 3b). $MAPbBr_3$ grown from S-AVC method showed a preferential orientation along [100] crystal plane, as given in Figure 3b. The full width half maximum of the [100] peak was 0.06^o indicating good crystallinity of the material (Figure S11). $MAPbI_3$ grown by S-AVC showed a preferred orientation along [310]. The material showed good crystallinity as the measured FWHM of the [110] peak was 0.06^o (Figure S12). The tightly packed pinhole free $MAPbI_3$ film was

composed of individual crystallites with an average dimension of 100µm. Since the material had superior crystallinity and reduced grain boundaries, the crystal film showed superior ambient stability (Figure S13) when compared to its thin film counterparts as explained by Wang *et al.*[13]

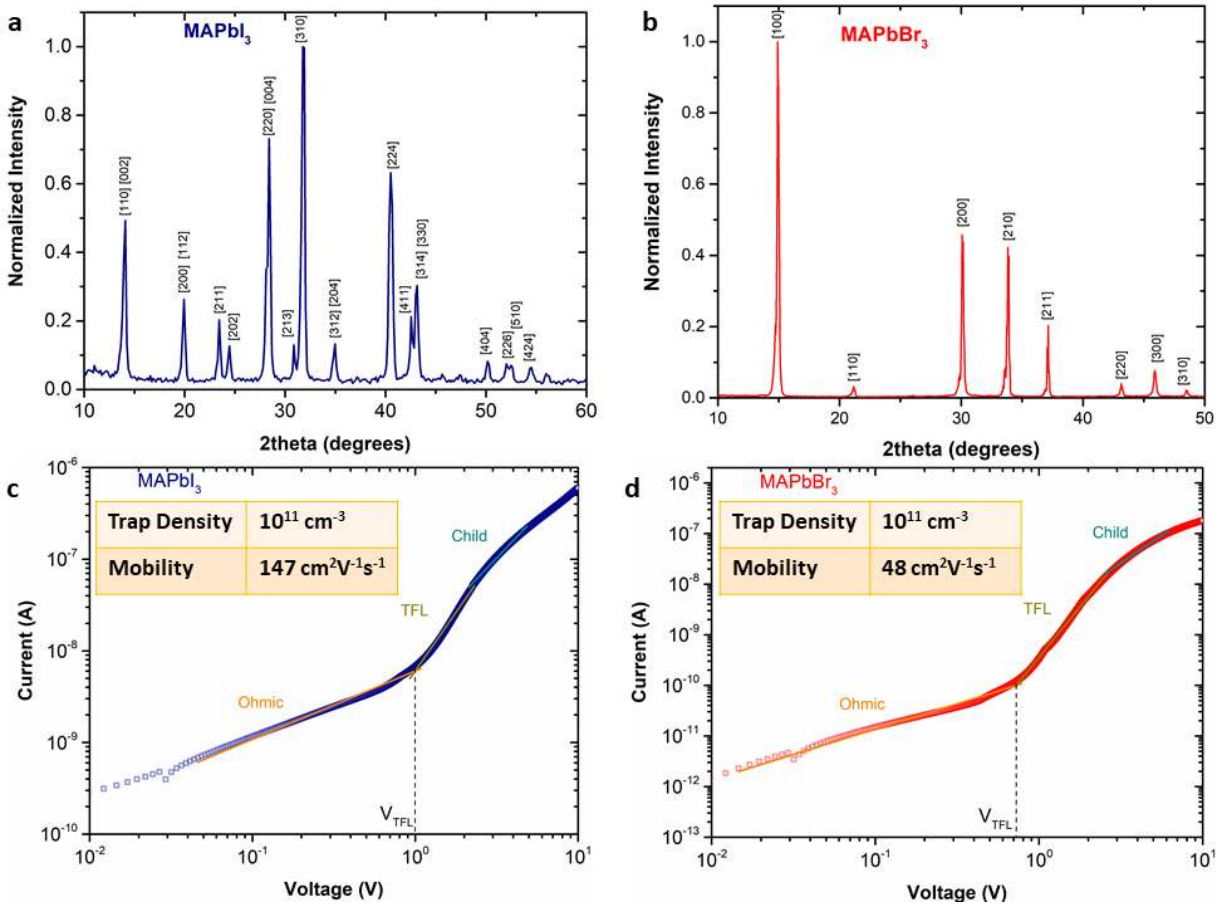

Figure 3. a) and b) XRD of S-AVC grown $MAPbI_3$ and $MAPbBr_3$ respectively. c) and d) SCLC based trap density measurements for $MAPbI_3$ and $MAPbBr_3$ respectively by growing crystals over pre-patterned FTO electrodes separated by 100µm. Inset shows the trap density values in comparison with the best thin film and single crystal values available from literatures.

To assess the quality of these crystal films, we carried out space charge limited current (SCLC) measurements and their trap densities were calculated (Figure 3c and 3d). Crystals were grown

over patterned fluorine doped tin oxide (FTO) electrodes which are relatively inert to lead halide perovskites, by S-AVC method as described above. Due to ionic nature of the material, a high inter-electrode spacing of 100 μm was chosen to keep a minimal electric field. The current–voltage characteristics was measured across the electrodes. A $\log_{10}V$ - $\log_{10}I$ curve was plotted to identify the trap filling voltage (V_{TFL}), characterized by a sudden increase in the current passed through the semiconductor.

The trap densities were calculated using the expression,

$$N_{traps} = \frac{2\varepsilon V_{TFL}}{qL^2} \quad \text{.....(1)}$$

Where ε is the dielectric constant of the material, L is the distance between the electrodes and q is the electronic charge. The dielectric constants (ε_r) were taken as 25.5 for $MAPbBr_3$ and 28.8 for $MAPbI_3$.[31] The measured trap densities were very low, of the order of 10^{11} cm^{-3}, for both $MAPbBr_3$ and $MAPbI_3$. These values are comparable to the values reported previously for their single crystal counterparts.[11,32] The electric current through the semiconductor at child region follows the equation,

$$J_{child} = \frac{9}{8}\ \varepsilon\mu\frac{V_a^2}{L^3} \quad \text{.....(2)}$$

Where J_{child} is the current density through the semiconductor at child region, μ is the mobility of the charge carriers and V_a is the applied voltage across the electrodes (Area of current flow is 5.8 mm x 400 nm). Substituting these values, the mobility of the charge carriers can be obtained as 48 $cm^2V^{-1}s^{-1}$ and 147 $cm^2V^{-1}s^{-1}$ for MAPbBr3 and MAPbI3 respectively.

The material also showed red shifted photoluminescence (PL) peaks when compared to their thin films (Figure S14). These are typical characteristics of single crystals of lead halide perovskites

which are attributed to the process of re-absorption of photoluminescence in the crystalline material.[32,33]

S-AVC based thick $MAPbI_3$ crystal photodetectors: The closely packed and pinhole free $MAPbI_3$ crystals grown over substrates can be efficiently used to fabricate planar optoelectronic devices. We induced the growth of $MAPbI_3$ crystals by S-AVC over laser etched and pre-patterned interdigitated FTO substrates to create planar photodetectors. The channel length between the electrodes was 100µm and the device had an active area of 3.17×10^{-6} m^2. The photodetectors thus formed were bottom illuminated from the glass side with a wavelength of 445 nm and was kept at a vacuum of 10^{-3} bar during all the measurements. As shown by the energy band diagram of the device (assuming the material to be intrinsic), the photo-generated electrons and holes will get swept across the semiconductor when an external bias is applied (Figure S15).

The current–voltage characteristics were non-linear (Figure 4a) indicating the presence of potential barriers between hybrid perovskite semiconductor and FTO electrodes. Owing to the superior crystallinity and large thickness of the grown perovskite crystals, the device generated very high photocurrents even for low power illumination (About 60µA for 3µW illumination). The high photocurrent values for our crystal devices can be qualitatively described by a device model explained in the supporting information. Two key parameters responsivity and detectivity are commonly used to determine the sensitivity of a photodetector.

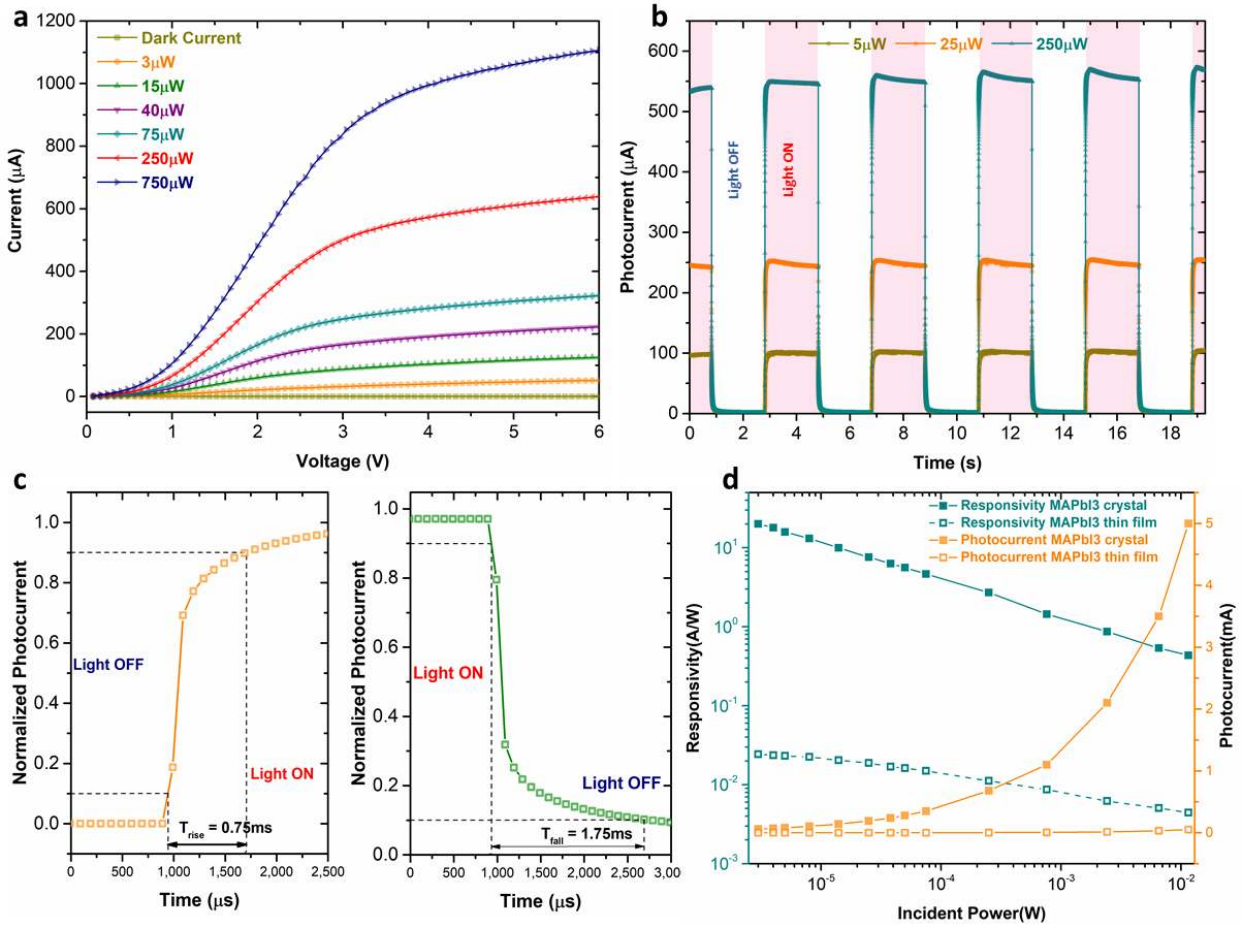

Figure 4. a) Photodetector I-V characteristics for various illumination power. b) Pulsed light characteristics for the device kept at a fixed bias of 8 V and irradiated with different power. c) Rise and fall time measurements for the device when illuminated with a pulsed light source of power 2.4 mW and biased at 8 V. d) Responsivity and photocurrent variation with varying incident light intensity.

The responsivity (R) of the photodetector can be calculated as,

$$R = \frac{J_{ph}}{\phi} = \frac{I_{ph}}{\phi s} \qquad \text{.....(3)}$$

Where, J_{ph} is the photocurrent density, ϕ the incident light intensity and s the active area of the photodetector. The measured Responsivity for the photodetector was 20 AW^{-1}.

Another figure of merit of the device, the detectivity (D*) can be calculated from the responsivity as, (by considering that the shot noise of the photodetector is significantly larger than flicker and Johnson noise)

$$D^* = \frac{R}{\sqrt{2qJ_{dark}}} = R\sqrt{\frac{s}{2qI_{dark}}} \qquad \text{.....(4)}$$

Where, J_{dark} is the dark current density of the device, I_{dark} the corresponding dark current and q the electronic charge. The calculated detectivity was 1.48 x 10^{13} Jones, a very high detectivity reported for a $MAPbI_3$ photoconductor (Table S3). Both the detectivity and responsivity was measured for an illumination power of 3 μW. The low dark current due to larger inter-electrode spacing and high responsivity owing to its superior crystallinity and absorption cross-section resulted in this impressive detectivity. Since crystal $MAPbI_3$ absorbs light in the entire visible spectrum and has a very high detectivity value (100 times larger than commercial Si photodetector), it can be considered as a promising candidate for low light imaging sensors. Over the same patterned substrate, a thin film of $MAPbI_3$ was coated by spin coating process to create a thin film photodetector. The calculated responsivity and detectivity for this photodetector was 0.02 AW^{-1} and 3 x 10^{10} Jones respectively (Figure S16). This indicates the nearly single crystal-like quality of the crystals gown over substrates. Since the photodetectors need to operate on continuously varying signals and must show excellent repeatability, the device was subjected to pulsed illuminations of wavelength 445 nm with different intensities (Figure 4b). The device yielded a decent ON- OFF ratio of 1.4 x 10^3 for an incident power of 2.4 mW. The rise-time and fall time for the device were calculated as 0.75 ms and 1.75 ms respectively, as given in Figure 4c. The usage of an inert conducting oxide (FTO) as electrode, a low electric field across the material and a highly crystalline perovskite as semiconductor yielded a highly stable and high sensitivity photoconductor photodetector (Figure 4d)

CONCLUSIONS

We investigated the mechanism of crystallization of lead halide perovskites by anti-solvent vapor crystallization and highlighted the importance of surface energy and the

heterogeneous nature of crystallization. Heterogeneous nucleation and three-dimensional growth results in the growth of millimeter sized perovskite crystals. The system moved to predominant homogenous nucleation when perturbed and then the crystallization proceeded in precursor 'dispersion' bulk. S-AVC deposition method can be utilized to grow crystals over any substrates, as the initial nucleation and growth of seed crystals were independent of substrate surfaces. The tightly packed and highly crystalline perovskite layers grown over substrates by S-AVC deposition method can be used to fabricate planar optoelectronic devices. A planar photodetector fabricated by this method yielded excellent responsivity as well as colossal detectivity for $MAPbI_3$ based photoconductors. In short, we demonstrated that a perturbed AVC system along with surface energy modification can result in the growth of substrate surface integrated lead halide perovskite crystals. This provides a simple and efficient approach to fabricate scalable, high performance planar optoelectronic devices with single crystal-like device characteristics.

ASSOCIATED CONTENT

Supporting Information.

The supporting information (pdf) includes experimental section, X-ray diffraction, FWHM of XRD, PL measurements, light scattering photographs, Dynamic Light Scattering measurements, SEM images, thin film photoconductor device measurements and its comparison table with crystal-based devices, performance comparison table of various photoconductors from literatures.

AUTHOR INFORMATION

Corresponding Author

Prof. Nripan Mathews (Email: Nripan@ntu.edu.sg)

Notes

The authors declare no competing financial interests.

ACKNOWLEDGMENT

This research was supported by the National Research Foundation, Prime Minister's Office, Singapore under its Competitive Research Programme (CRP Award No. NRF-CRP14-2014-03) and through the Singapore–Berkeley Research Initiative for Sustainable Energy (SinBeRISE) CREATE Program. The authors also acknowledge funding from Office of Naval Research Global (ONRG-NICOP-N62909-17-1-2155). The intensity dependent time correlated single photon counting of the fluorescence emission was performed by the centre of biophysics at SPMS, supported by NTU Singapore.

REFERENCES

(1) Brandt, R. E.; Stevanović, V.; Ginley, D. S.; Buonassisi, T. Identifying Defect-Tolerant Semiconductors with High Minority-Carrier Lifetimes: Beyond Hybrid Lead Halide Perovskites. *MRS Commun.* **2015**, *5* (02), 265–275. https://doi.org/10.1557/mrc.2015.26.

(2) Grätzel, M. The Light and Shade of Perovskite Solar Cells. *Nat. Publ. Gr.* **2014**, *13* (9), 838–842. https://doi.org/10.1038/nmat4065.

(3) Veldhuis, S. A.; Boix, P. P.; Yantara, N.; Li, M.; Sum, T. C.; Mathews, N.; Mhaisalkar, S. G. Perovskite Materials for Light-Emitting Diodes and Lasers. *Adv. Mater.* **2016**, 6804–6834. https://doi.org/10.1002/adma.201600669.

(4) Fang, Y.; Dong, Q.; Shao, Y.; Yuan, Y.; Huang, J. Highly Narrowband Perovskite Single-Crystal Photodetectors Enabled by Surface-Charge Recombination. *Nat. Photonics* **2015**, *9* (10), 679–686. https://doi.org/10.1038/nphoton.2015.156.

(5) Xu, W.; Cho, H.; Kim, Y. H.; Kim, Y. T.; Wolf, C.; Park, C. G.; Lee, T. W. Organometal Halide Perovskite Artificial Synapses. *Adv. Mater.* **2016**, 5916–5922. https://doi.org/10.1002/adma.201506363.

(6) Senanayak, S. P.; Yang, B.; Thomas, T. H.; Giesbrecht, N.; Huang, W.; Gann, E.; Nair, B.; Goedel, K.; Guha, S.; Moya, X.; et al. Understanding Charge Transport in Lead Iodide Perovskite Thin-Film Field-Effect Transistors. *Sci. Adv.* **2017**, *3* (1), e1601935. https://doi.org/10.1126/sciadv.1601935.

(7) Cho, N.; Li, F.; Turedi, B.; Sinatra, L.; Sarmah, S. P.; Parida, M. R.; Saidaminov, M. I.; Murali, B.; Burlakov, V. M.; Goriely, A.; et al. Pure Crystal Orientation and Anisotropic Charge Transport in Large-Area Hybrid Perovskite Films. *Nat. Commun.* **2016**, *7* (May), 13407. https://doi.org/10.1038/ncomms13407.

(8) Saidaminov, M. I.; Adinolfi, V.; Comin, R.; Abdelhady, A. L.; Peng, W.; Dursun, I.; Yuan, M.; Hoogland, S.; Sargent, E. H.; Bakr, O. M. Planar-Integrated Single-Crystalline Perovskite Photodetectors. *Nat Commun* **2015**, *6*, 8724. https://doi.org/10.1038/ncomms9724.

(9) Shi, D.; Adinolfi, V.; Comin, R.; Yuan, M.; Alarousu, E.; Buin, A.; Chen, Y.; Hoogland, S.; Rothenberger, A.; Katsiev, K.; et al. Low Trap-State Density and Long Carrier Diffusion in Organolead Trihalide Perovskite Single Crystals. *Science (80-.).* **2015**, *347* (6221), 519–522. https://doi.org/10.1126/science.aaa2725.

(10) Dong, Q.; Fang, Y.; Shao, Y.; Mulligan, P.; Qiu, J.; Cao, L.; Huang, J. Electron-Hole Diffusion Lengths > 175 m m in Solution-Grown CH 3 NH 3 PbI 3 Single Crystals. *Science (80-.).* **2015**, *347* (6225), 967–970.

(11) Saidaminov, M. I.; Abdelhady, A. L.; Murali, B.; Alarousu, E.; Burlakov, V. M.; Peng, W.; Dursun, I.; Wang, L.; He, Y.; Maculan, G.; et al. High-Quality Bulk

Hybrid Perovskite Single Crystals within Minutes by Inverse Temperature Crystallization. *Nat. Commun.* **2015**, *6* (May), 7586. https://doi.org/10.1038/ncomms8586.

(12) Stolterfoht, M.; Wolff, C. M.; Márquez, J. A.; Zhang, S.; Hages, C. J.; Rothhardt, D.; Albrecht, S.; Burn, P. L.; Meredith, P.; Unold, T.; et al. Visualization and Suppression of Interfacial Recombination for High-Efficiency Large-Area Pin Perovskite Solar Cells. *Nat. Energy* **2018**, *3* (10), 847–854. https://doi.org/10.1038/s41560-018-0219-8.

(13) Wang, Q.; Chen, B.; Liu, Y.; Deng, Y.; Bai, Y.; Dong, Q.; Huang, J. Scaling Behavior of Moisture-Induced Grain Degradation in Polycrystalline Hybrid Perovskite Thin Films. *Energy Environ. Sci.* **2017**, *10* (2), 516–522. https://doi.org/10.1039/C6EE02941H.

(14) Levine, I.; Nayak, P. K.; Wang, J. T. W.; Sakai, N.; Van Reenen, S.; Brenner, T. M.; Mukhopadhyay, S.; Snaith, H. J.; Hodes, G.; Cahen, D. Interface-Dependent Ion Migration/Accumulation Controls Hysteresis in MAPbI3 Solar Cells. *J. Phys. Chem. C* **2016**, *120* (30), 16399–16411. https://doi.org/10.1021/acs.jpcc.6b04233.

(15) Yun, J. S.; Seidel, J.; Kim, J.; Soufiani, A. M.; Huang, S.; Lau, J.; Jeon, N. J.; Seok, S. Il; Green, M. A.; Ho-Baillie, A. Critical Role of Grain Boundaries for Ion Migration in Formamidinium and Methylammonium Lead Halide Perovskite Solar Cells. *Adv. Energy Mater.* **2016**, *6* (13), 1–8. https://doi.org/10.1002/aenm.201600330.

(16) Shao, Y.; Fang, Y.; Li, T.; Wang, Q.; Dong, Q.; Deng, Y.; Yuan, Y.; Wei, H.; Wang, M.; Gruverman, A.; et al. Grain Boundary Dominated Ion Migration in Polycrystalline Organic–Inorganic Halide Perovskite Films. *Energy Environ. Sci.* **2016**, *9* (5), 1752–1759. https://doi.org/10.1039/C6EE00413J.

(17) Rolston, N.; Watson, B. L.; Bailie, C. D.; McGehee, M. D.; Bastos, J. P.; Gehlhaar, R.; Kim, J. E.; Vak, D.; Mallajosyula, A. T.; Gupta, G.; et al. Mechanical Integrity of Solution-Processed Perovskite Solar Cells. *Extrem. Mech. Lett.* **2016**, *9*, 353–358. https://doi.org/10.1016/j.eml.2016.06.006.

(18) Feng, J. Mechanical Properties of Hybrid Organic-Inorganic $CH_3NH_3BX_3$ (B = Sn, Pb; X = Br, I) Perovskites for Solar Cell Absorbers. *APL Mater.* **2014**, *2* (8), 081801. https://doi.org/10.1063/1.4885256.

(19) Chen, Z.; Turedi, B.; Alsalloum, A.; Yang, C.; Zheng, X.; Gereige, I.; AlSaggaf, A.; Mohammed, O. F.; Bakr, O. M. Single-Crystal MAPbI3 Perovskite Solar Cells Exceeding 21% Power Conversion Efficiency. *ACS Energy Lett.* **2019**, 1258–1259. https://doi.org/10.1021/acsenergylett.9b00847.

(20) Peng, W.; Wang, L.; Murali, B.; Ho, K. T.; Bera, A.; Cho, N.; Kang, C. F.; Burlakov, V. M.; Pan, J.; Sinatra, L.; et al. Solution-Grown Monocrystalline Hybrid Perovskite Films for Hole-Transporter-Free Solar Cells. *Adv. Mater.* **2016**, *28* (17), 3383–3390. https://doi.org/10.1002/adma.201506292.

(21) Saidaminov, M. I.; Adinolfi, V.; Comin, R.; Abdelhady, A. L.; Peng, W.; Dursun, I.; Yuan, M.; Hoogland, S.; Sargent, E. H.; Bakr, O. M. Planar-Integrated Single-Crystalline Perovskite Photodetectors. *Nat. Commun.* **2015**, *6*, 8724. https://doi.org/10.1038/ncomms9724.

(22) Yan, K.; Long, M.; Zhang, T.; Wei, Z.; Chen, H.; Yang, S.; Xu, J. Hybrid Halide Perovskite Solar Cell Precursors: Colloidal Chemistry and Coordination Engineering behind Device Processing for High Efficiency. *J. Am. Chem. Soc.* **2015**, *137* (13), 4460–4468. https://doi.org/10.1021/jacs.5b00321.

(23) Pratap, S.; Keller, E.; Müller-Buschbaum, P. Emergence of Lead Halide Perovskite Colloidal Dispersions through Aggregation and Fragmentation:

Insights from the Nanoscale to the Mesoscale. *Nanoscale* **2019**, *11* (8), 3495–3499. https://doi.org/10.1039/c8nr09853k.

(24) Zijlema, T. G.; Oosterhof, H.; Witkamp, G. J.; Rosmalen, G. M. Van. Crystallization of Sodium Chloride with Amines as Antisolvents. **1997**, No. 7, 230–241. https://doi.org/10.1016/j.cej.2005.01.001.

(25) Oosterhof, H. Antisolvent Crystallization of Anhydrous Sodium Carbonate at Atmospherical Conditions. **2001**, *47* (3).

(26) S. Mostafa Nowee, Ali Abbas, J. A. R. Antisolventcrystallization Model Identification, Experimental Validation Anddynamic.

(27) Haller, I. Covalently Attached Organic Monolayers on Semiconductor Surfaces. *J. Am. Chem. Soc.* **1978**, *100* (26), 8050–8055. https://doi.org/10.1021/ja00494a003.

(28) Acres, R. G.; Ellis, A. V.; Alvino, J.; Lenahan, C. E.; Khodakov, D. A.; Metha, G. F.; Andersson, G. G. Molecular Structure of 3-Aminopropyltriethoxysilane Layers Formed on Silanol-Terminated Silicon Surfaces. *J. Phys. Chem. C* **2012**, *116* (10), 6289–6297. https://doi.org/10.1021/jp212056s.

(29) Zeng, X.; Xu, G.; Gao, Y.; An, Y. Surface Wettability of (3-Aminopropyl)Triethoxysilane Self-Assembled Monolayers. *J. Phys. Chem. B* **2011**, *115* (3), 450–454. https://doi.org/10.1021/jp109259b.

(30) Tillman, N.; Ulman, A.; Schildkraut, J. S.; Penner, T. L. Incorporation of Phenoxy Groups in Self-Assembled Monolayers of Trichlorosilane Derivatives: Effects on Film Thickness, Wettability, and Molecular Orientation. *J. Am. Chem. Soc.* **1988**, *110* (18), 6136–6144. https://doi.org/10.1021/ja00226a031.

(31) Poglitsch, A.; Weber, D. Dynamic Disorder in Methylammoniumtrihalogenoplumbates (II) Observed by Millimeter-wave

Spectroscopy. *J. Chem. Phys.* **1987**, *87* (11), 6373–6378. https://doi.org/10.1063/1.453467.

(32) Yamada, T.; Yamada, Y.; Nakaike, Y.; Wakamiya, A.; Kanemitsu, Y. Photon Emission and Reabsorption Processes in CH3NH3PbBr3 Single Crystals Revealed by Time-Resolved Two-Photon-Excitation Photoluminescence Microscopy. *Phys. Rev. Appl.* **2017**, *7* (1), 1–8. https://doi.org/10.1103/PhysRevApplied.7.014001.

(33) Wu, B.; Nguyen, H. T.; Ku, Z.; Han, G.; Giovanni, D.; Mathews, N.; Fan, H. J.; Sum, T. C. Discerning the Surface and Bulk Recombination Kinetics of Organic–Inorganic Halide Perovskite Single Crystals. *Adv. Energy Mater.* **2016**, *6* (14), 1–9. https://doi.org/10.1002/aenm.201600551.

Supporting Information

Perturbation Induced Seeding and Crystallization of Hybrid Perovskites Over Surface Modified Substrates for Optoelectronic Devices

Riyas Ahmad[a,b,c], Abhijith Surendran[e], P. C. Harikesh[a,b,d], Haselsberger Reinhard[c], Nur Fadilah Jamaludin[a,b,d], Rohit Abraham John[d], Teck Ming Koh[a], Annalisa Bruno[a], Wei Lin Leong[e,f], Nripan Mathews[a,d], Maria-Elisabeth Michel-Beyerle[c] and Subodh G. Mhaisalkar[a,d]*

g. Energy Research Institute at NTU (ERI@N), Research Techno Plaza, X-Frontier Block Level 5, 50 Nanyang Drive, Singapore 637553.
h. Interdisciplinary Graduate School (IGS), Nanyang Technological University, 50 Nanyang Avenue, Singapore 639798.
i. Division of Physics and Applied Physics, School of Physical and Mathematical Sciences (SPMS), Nanyang Technological University, 21 Nanyang Link, Singapore 637371.
j. School of Materials Science and Engineering, Nanyang Technological University, 50 Nanyang Avenue, Singapore 639798.
k. School of Electrical and Electronic Engineering, Nanyang Technological University, 50 Nanyang Avenue, Singapore 639798.
l. School of Chemical and Biomedical Engineering, Nanyang Technological University, 70 Nanyang Drive, Singapore 637459.

***Corresponding Author**

Prof. Nripan Mathews (Email: Nripan@ntu.edu.sg)

EXPERIMENTAL SECTION

1. Sonication modified Growth of Perovskite Crystals on Substrates (S-AVC)

In Antisolvent Vapor Crystallization (AVC) process, as discussed earlier,[1] the anti-solvent vapor is allowed to slowly evaporate to the solvent precursor solution, which creates supersaturation and crystallization. The crystal growth system has to be kept vibration free for better crystal growth to take place.

Here, the process recipe was fine tuned for $MAPbBr_3$ and $MAPbI_3$ as given in the Table S1 to get a uniform crystal growth and coverage over the substrate surface. For $MAPbBr_3$ crystals, we dissolved 0.20M $PbBr_2$ and 0.20M MABr in 10ml Dimethylformamide (DMF) to form the precursor solution. For $MAPbI_3$, 0.20M PbI_2 and 0.24M MAI were dissolved in γ-Butyrolactone (GBL) to form the precursor. The precursor solutions were filtered using 0.2µm PTFE filter and transferred to a 50ml crystallization dish with OTS SAM modified surfaces. The substrates on which the crystals have to be grown are cleaned in soap solution, dilute acid, water, acetone, deionized water and ethanol followed by nitrogen blowing. The cleaned substrates were ozone treated and surface modified with APTMS before dipping them in the precursor solution kept in the crystallization dish. The crystallization dish was sealed and a hole of approximate cross section of 0.5mm was provided for the antisolvent to diffuse into it. The precursor solution and substrate containing crystallization dish is kept inside a 250ml beaker with 50ml Dichloromethane (DCM) inside. The outer 250ml beaker is tightly sealed so that the DCM, upon evaporation moves to the crystallization dish kept inside through the tiny hole provided. As the antisolvent moves to the precursor solution it creates supersaturation inside and the crystals just start growing. The crystallization process is very slow and usually starts forming crystals in 3 days. A short ultrasound pulse of 500W (duration of 1 second) was applied using a bath sonication apparatus on the crystallization solution at deep supersaturation, when tiny crystals were just forming. The ultrasound creates cavitation and microbubble formation inside the precursor solution. The imploding of these microbubbles provides sufficient energy to overcome the nucleation barrier. The numerous tiny microcrystals formed as a result of nucleation in the solution will get attached to the high energy substrate surfaces. Upon

further introduction of antisolvent vapor the crystal seeds on the substrate grows in three dimensions to cover the entire substrate.

Table S1: The sonication modified antisolvent vapor crystallization recipe for $MAPbBr_3$ and $MAPbI_3$.

Crystal Grown	Precursor Solvent	Precursor Ratio	Anti-solvent Used
$MAPbBr_3$	N, N-Dimethylformamide	0.20M $PbBr_2$ 0.20M MABr	Dichloromethane
$MAPbI_3$	γ-Butyrolactone	0.20M PbI_2 0.24M MAI	Dichloromethane

After the crystal growth, the substrates were taken out and were annealed at 80°C for 10 minutes and subsequently at 100°C for 10 minutes. All these procedures were carried out at room ambience.

The thin films used as references in the work used 1M precursors (MABr and $PbBr_2$ in DMF for $MAPbBr_3$; MAI and PbI_2 in DMF for $MAPbI_3$) and was spin coated along with solvent engineering process reported previously in literatures.[2]

All the processes used 99% pure MABr and MAI from Dyesol, 99.9% pure PbI2 from TCI, 99% pure PbBr2 from Sigma Aldrich. All the solvents were from Sigma Aldrich.

2. Surface modification of substrates and crystallization dish

The glass substrates were cleaned with decon solution, dilute HCl, water, DI water, acetone, ethanol and were dried under nitrogen blowing. The substrates were UV- ozone cleaned for 30 minutes prior to incubation. 10 µl of APTMS was dispersed in 10 ml of anhydrous ethanol and kept in a well cleaned glass incubation petri dish. The UV- ozone cleaned substrates were quickly transferred to the petri dish and kept undisturbed at room ambience for 20 minutes. After 20 minutes the substrates were taken out and were cleaned by anhydrous ethanol by placing it in the bath sonicator for 10 minutes. The substrates were later dried by nitrogen blowing.

The crystallization dishes were cleaned as per the same procedure described for the glass substrates. 4 µl of OTS was dispersed in 20 ml of anhydrous toluene and was poured into the crystallization dishes which were UV – ozone cleaned for 30 minutes. The crystallization dishes were closed and kept in room ambience undisturbed for 2 hours. After 2 hours the toluene containing OTS was poured out of the crystallization dish and cleaned thrice by rinsing with fresh toluene. The glass wares were dried under nitrogen blowing and kept in a drying oven (at 70 ^{o}C) for 2 hours.

All these chemicals were from Sigma Aldrich and were used without any further purification.

Precursor Solution Investigations

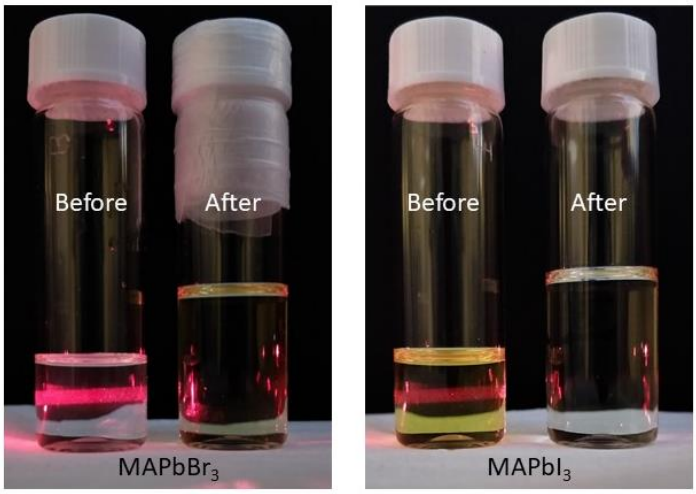

Figure S1: Precursors for $MAPbBr_3$ and $MAPbI_3$ before and after crystallization and scattering a laser beam of 650 nm.

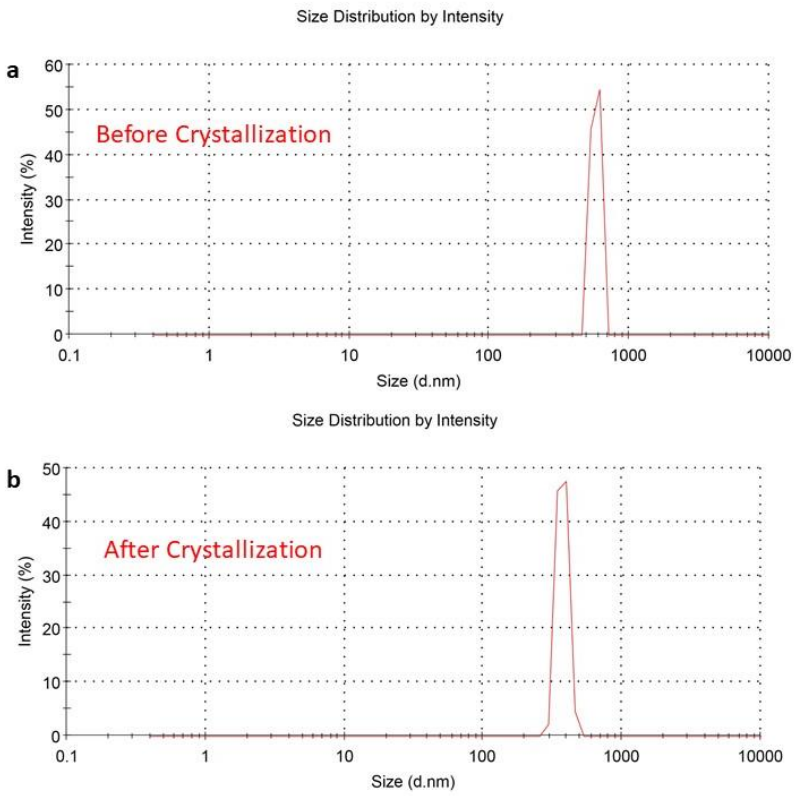

Figure S2: The DLS measurement curves for MAPbBr3 precursor in DMF before (colloidal size: 450 nm – 750 nm) and after crystallization. The colloidal sizes reduce (to 250 nm – 450 nm) after crystallization (after 60 hours of anti-solvent introduction)

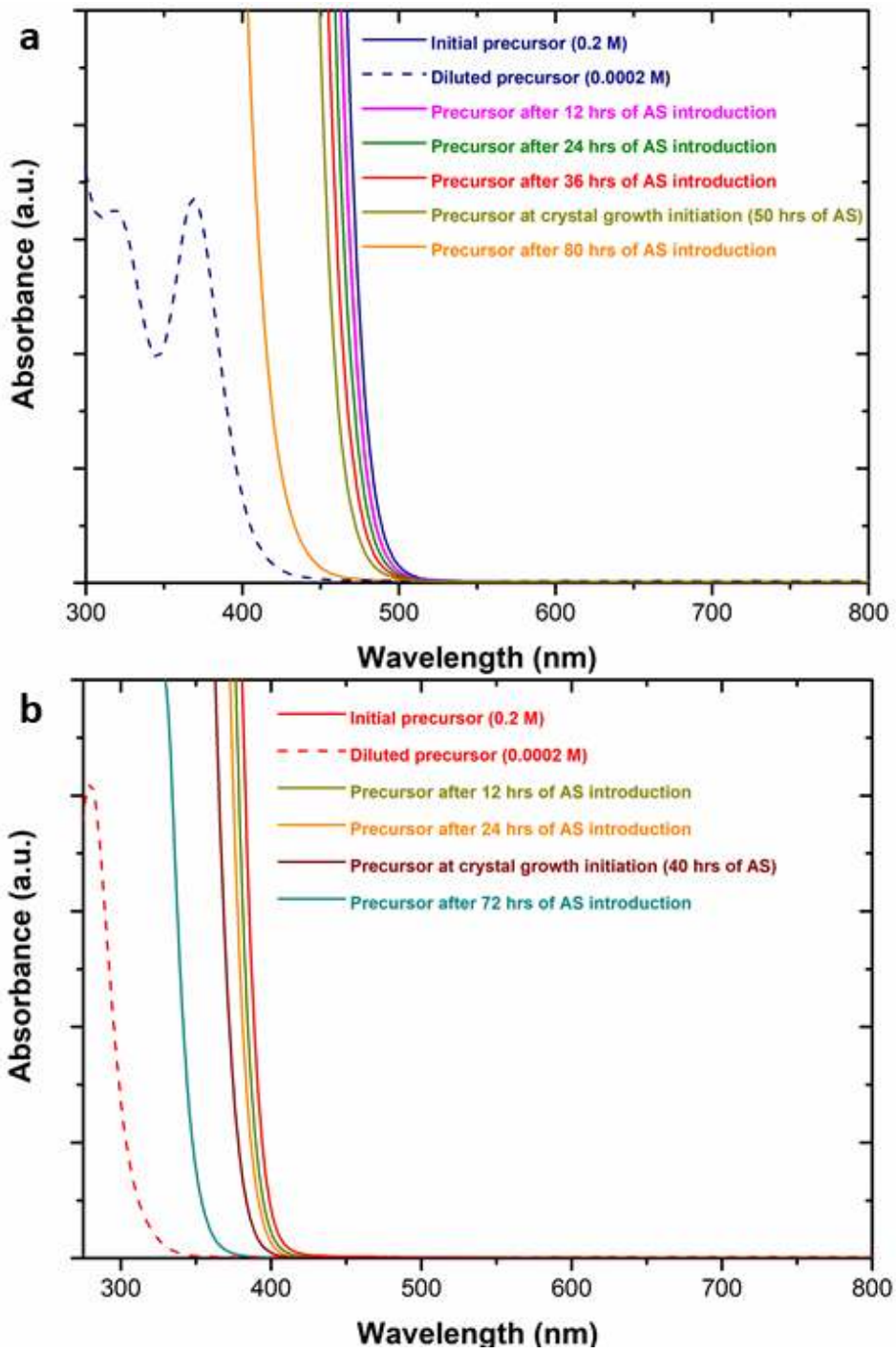

Figure S3: UV- Visible absorption spectra of (a) $MAPbI_3$ and (b) $MAPbBr_3$ precursors before, during and after crystallization.

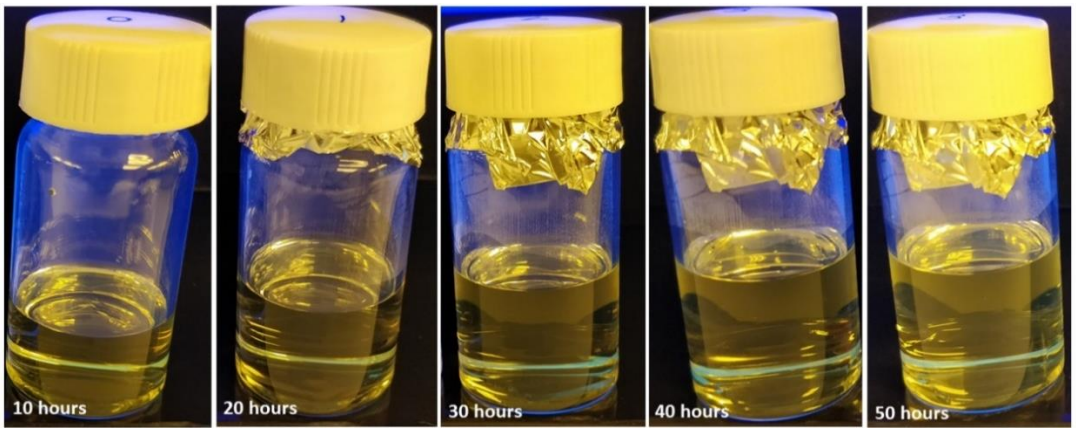

Figure S4: $MAPbI_3$ precursors illuminated by a UV source after different durations of anti-solvent introduction. The precursors didn't show any traces of colloidal perovskite crystal photoluminescence (PL).

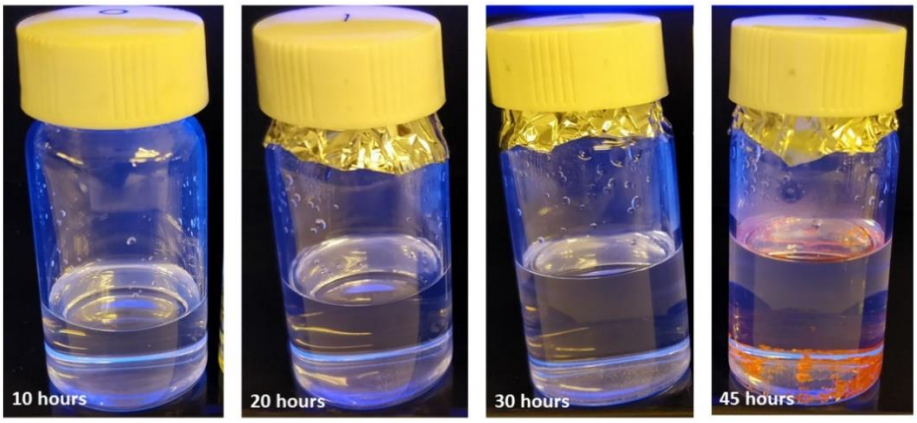

Figure S5: MAPbBr3 precursors showing no PL after different durations of anti-solvent introduction

Scheme 1: Mechanism of Antisolvent Vapour Crystallization

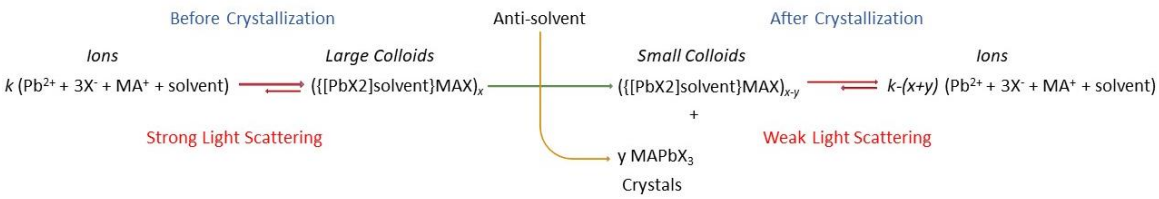

Morphology and Cross-section Investigations for the Crystals

The SEM images were obtained on JEOL Field Emission microscope JSM-7600F. The samples to be imaged are platinum sputtered to reduce the charging effect during the imaging process. The accelerating voltage was kept at 5kV for all the measurements.

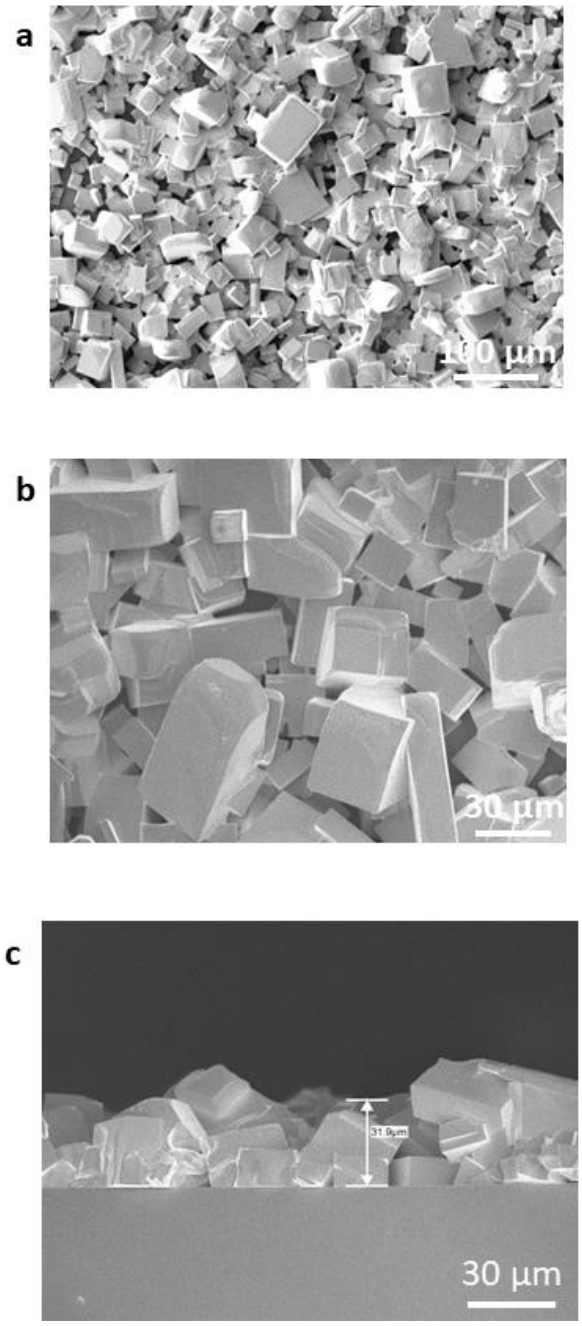

Figure S6: (a) and (b) SEM images of MAPbBr3 crystals grown over glass. (c) The cross section of the crystal film.

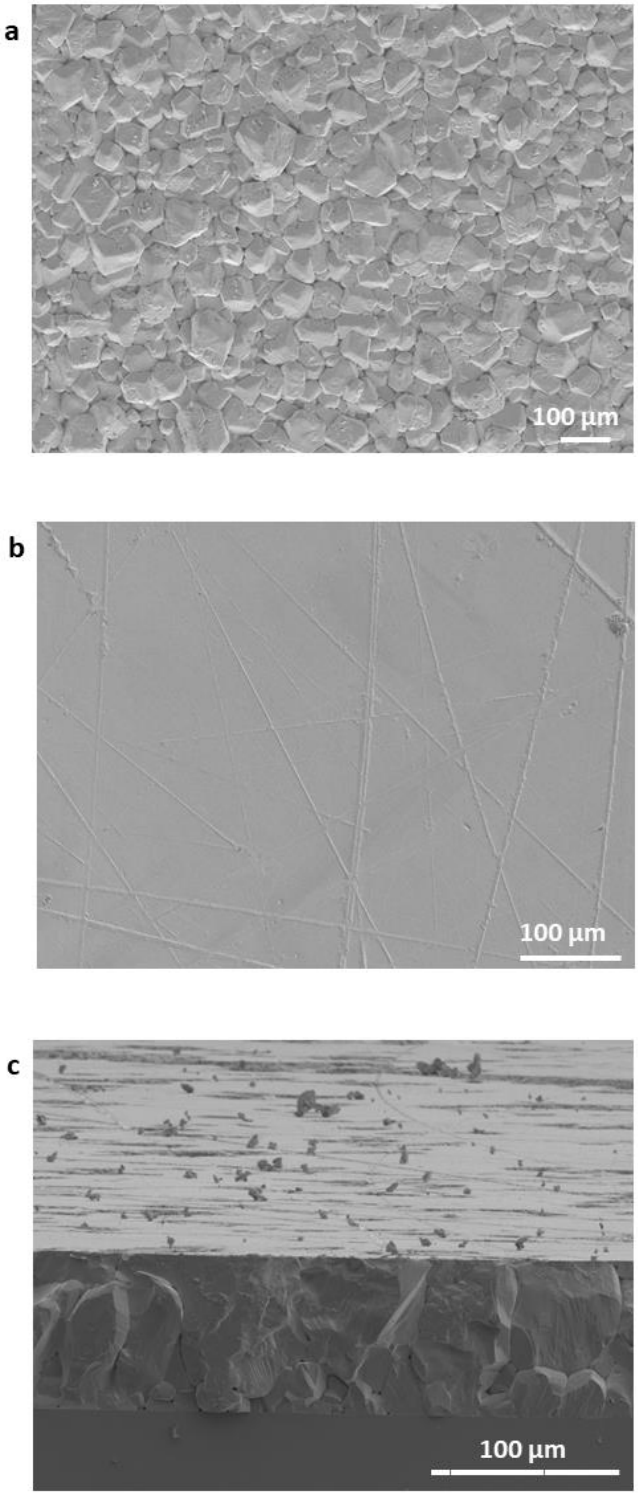

Figure S7: (a) SEM image of the surface of $MAPbI_3$ crystals grown over glass. (b) The crystal film surface after being polished by an optical sandpaper and its cross-section (c).

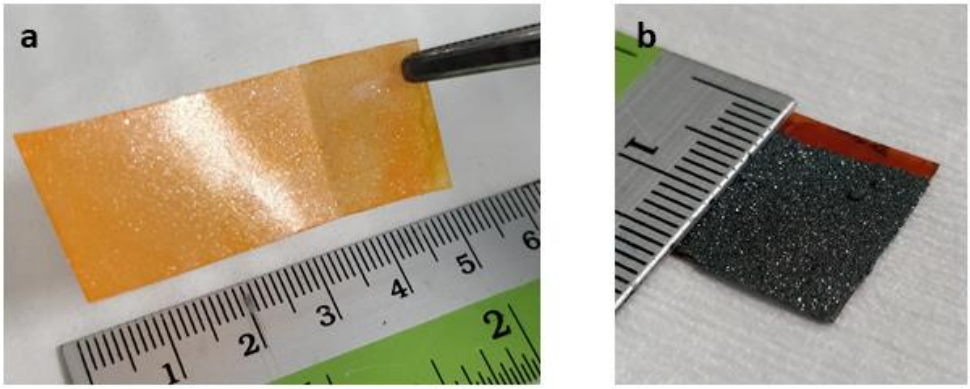

Figure S8: (a) $MAPbBr_3$ crystals grown over a curved PET substrate. (b) $MAPbI_3$ crystals grown over a Kapton sheet.

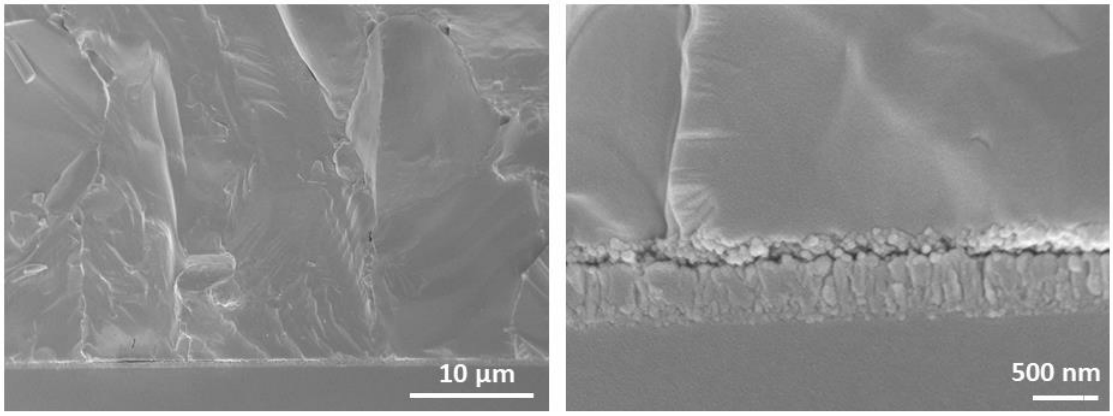

Figure S9: Cross sectional SEM images of the surface of $MAPbI_3$ crystals grown over mesoporous TiO2 layer, showing that the crystal growth process is independent of substrate surfaces.

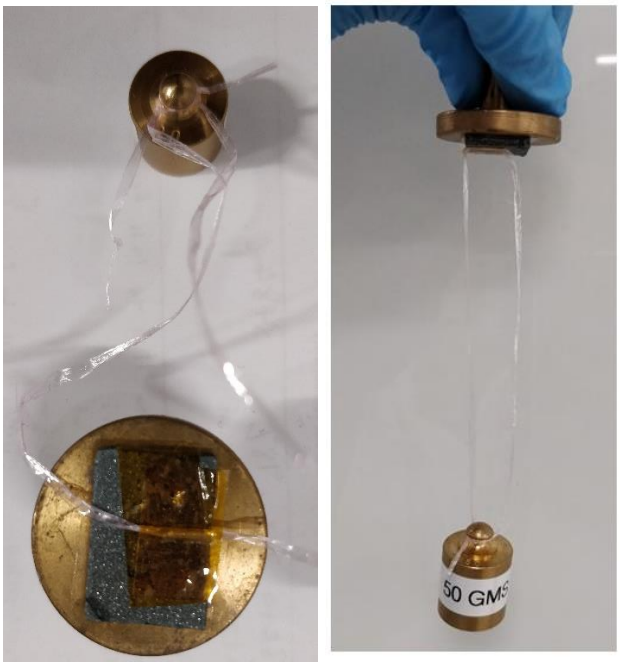

Figure S10: Tensile force applied by using a 50g standard weight on $MAPbI_3$ crystals grown over FTO substrates.

Crystallinity and Orientation Investigations

The crystallinity, orientation and morphology of the grown crystals on substrates were investigated using Scanning Electron Microscopy (SEM) and X- Ray Diffractometry (XRD). XRD patterns were obtained on Bruker D8 Advance diffractometer with a Cu target. K_α of X-Rays produced were of wavelength 1.5418 A^o at 40 kV and 40mA. The step size used for measuring the crystallinity (by Full Width Half Maximum) was 0.005 degrees with a step duration of 1.5 seconds.

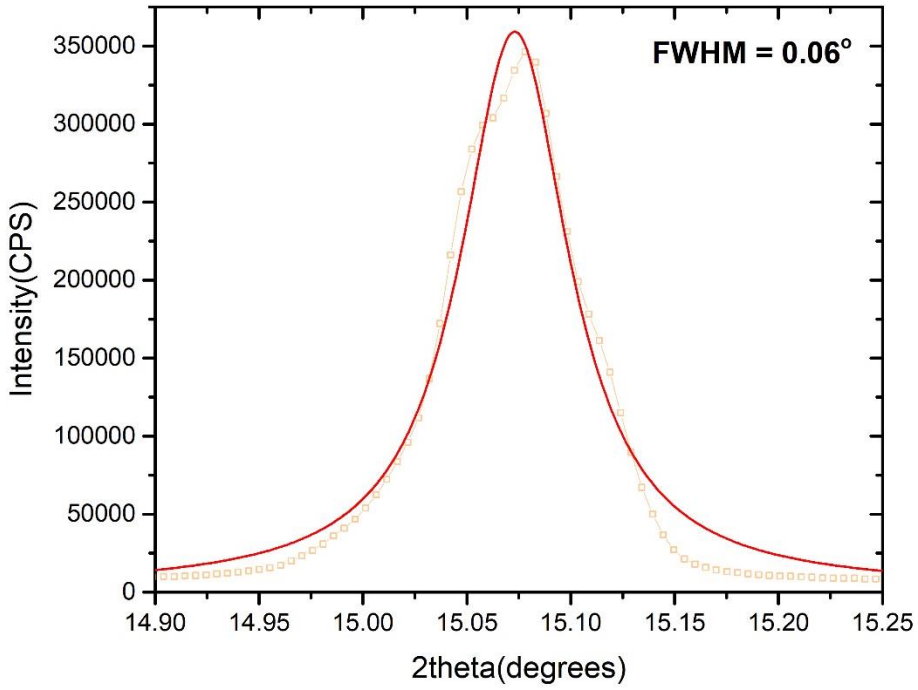

Figure S11: FWHM of [100] XRD peak of $MAPbBr_3$ grown by S-AVC on glass.

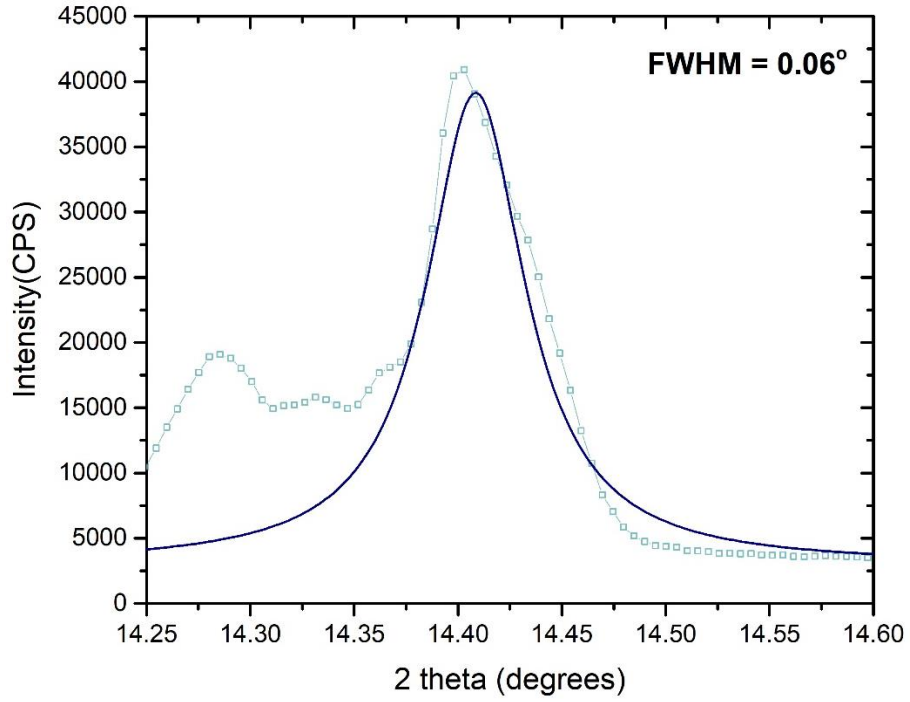

Figure S12: FWHM of [110] XRD peak of $MAPbI_3$ grown by S-AVC on glass.

Ambient Stability Studies

For measuring the ambient stability, a quick scan was used with 0.04 step size and 1 second step duration. Both the crystal film and thin film were stored in room ambience, at a temperature of 23°C and relative humidity of 75%

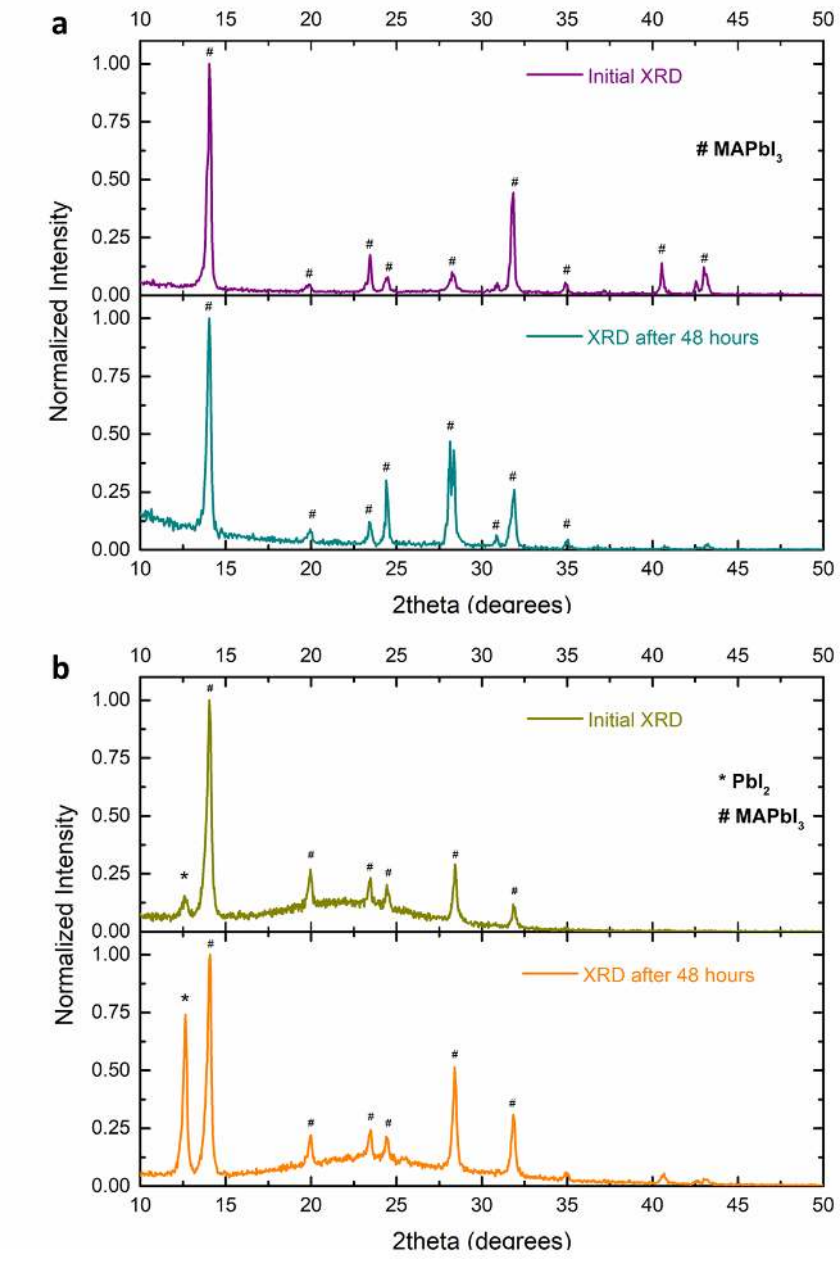

Figure S13: (a) XRD for $MAPbI_3$ crystals grown over glass and its variation after being kept at room ambience and (b) the corresponding data for spin coated $MAPbI_3$ thin film.

Photoluminescence Measurements

Steady state photoluminescence was measured using HORIBA Scientific Fluoromax-4 Spectro-fluorometer.

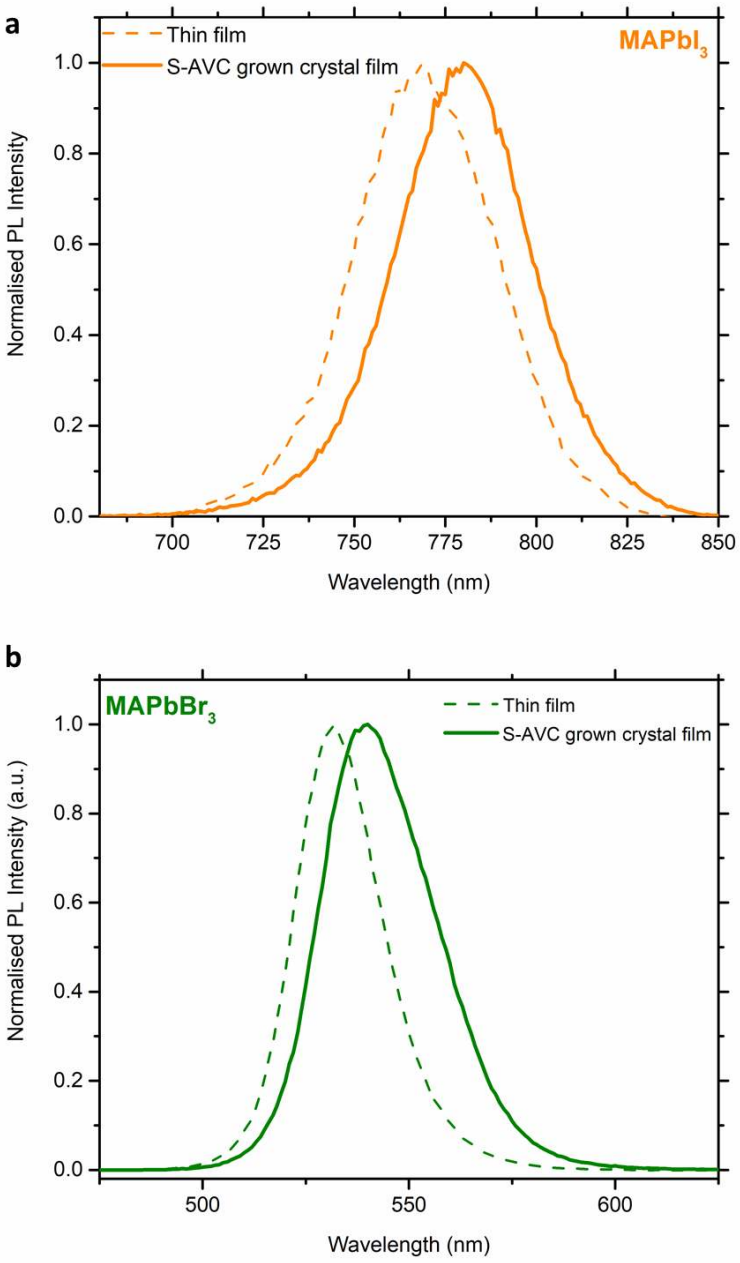

Figure S14: Photoluminescence spectra of (a) $MAPbI_3$ and (b) $MAPbBr_3$ showing redshifted maxima, when compared to their thin film counterparts.

Space Charge Limited Current Based Measurements

Pre-patterned interdigitated FTO electrodes deposited over glass substrate were used to conduct the SCLC measurements. After cleaning them, the substrates were used to grow crystals over them. The cleaned substrates were dipped in perovskite precursor solution and crystals were grown by the sonication modified growth technique as discussed before. SCLC measurement was carried out over this substrate integrated crystals to measure the trap density. A probe station and Keithley-4200 Semiconductor Characterization System was used to record the Voltage (V) - Current (I) curve. A $\log_{10}V$ - $\log_{10}I$ curve was plotted to identify the trap filling voltage (V_{TFL}), characterized by a sudden increase in the current passed through the semiconductor.

Fabrication and Characterizations of Photodetectors

The FTO substrates with interdigitated electrodes were patterned by laser etching. The channel length used was 100µm with a width of 3.17cm. The perovskite films were spun coated and the crystals were grown over this prepatterned substrate to create the photodetector.

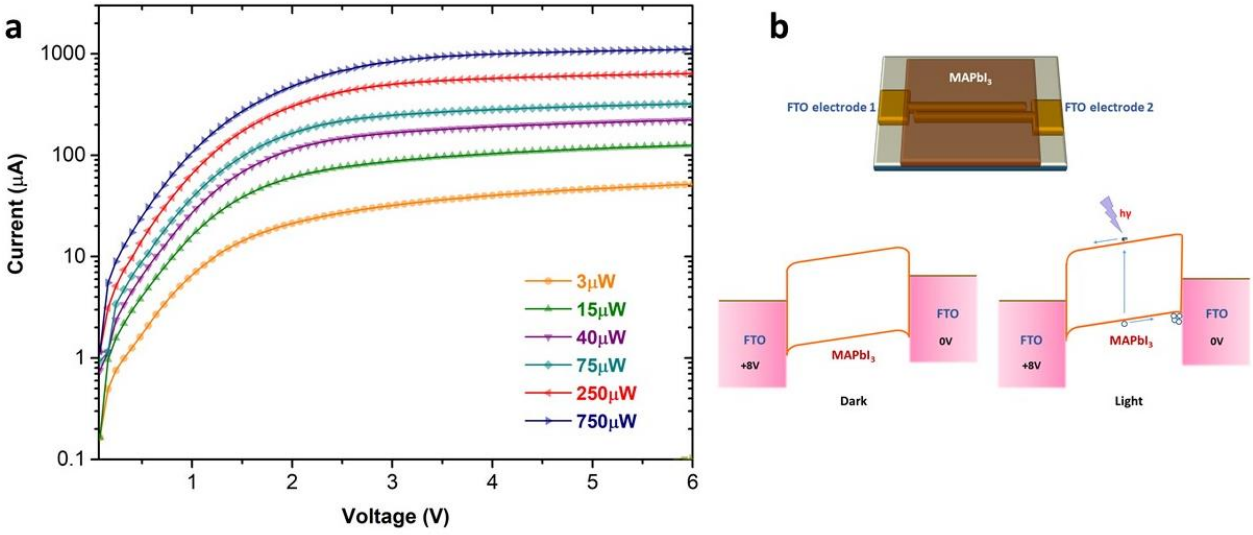

Figure S15: (a)Log I – V curve indicating the contact barrier in the device. (b) Energy band diagram of the device under bias, assuming the material to be intrinsic.

The incident light power on the device were varied from 3 µW to 10^4 µW and pulsed using a Thorlabs DC2200 LED driver and Solis-445C blue light LED source. The device characteristics were measured by using a Keithley 4200 SCS with the help of a probe station. The risetime and fall time were measured by using a Keysight B2912A Precision Source/Measure Unit, to achieve a better time resolution.

As shown by the energy band diagram of the device (assuming the material to be intrinsic), the photo-generated electrons and holes will get swept across the semiconductor when an external bias is applied. The log I- V plot indicates the formation of contact barriers between FTO and MAPbI3.

FTO – MAPbI3 junction creates a rectifying junction and hence the photoconductor has two Schottky barriers within the device. While applying a bias the device can be modelled as a combination of a diode and a resistor connected in series, which is evident from the log I- V curve.

As the biasing voltages are applied the methylammonium cations and iodide anions can accumulate at respective electrode perovskite junctions, leading to giant current amplification in the device, which enhances the photocurrent.[3]

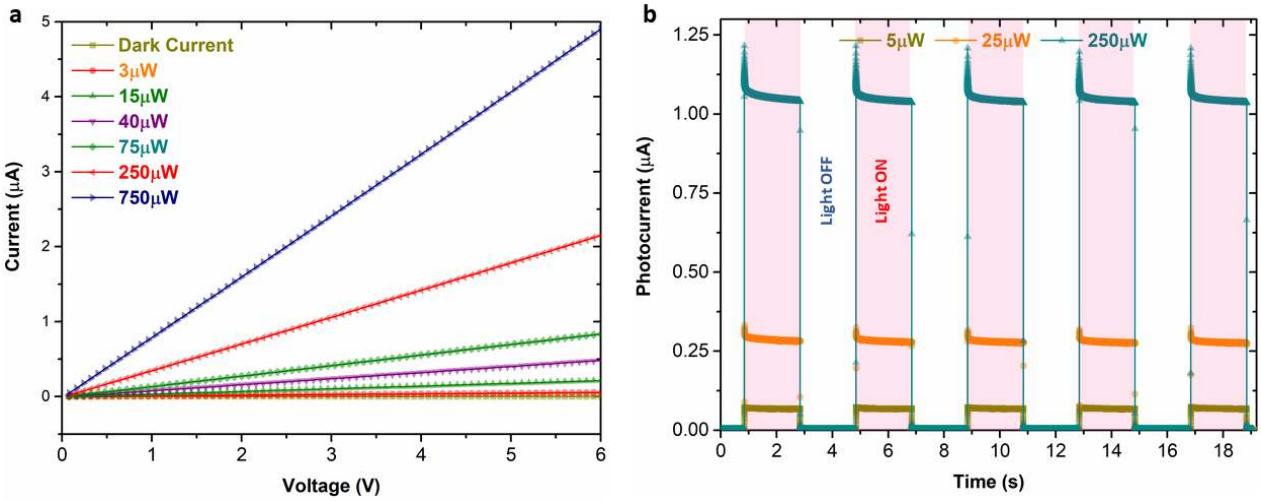

Figure S16: Photodetector response of a normal thin film MAPbI3 based device made on the same substrate. (a) V-I characteristics of the device. (b) Pulsed light characteristics for a biasing voltage of 8V.

Table S2: Performance comparison of photodetectors

Light Absorber	Responsivity (R)	Detectivity (D*)
$MAPbI_3$ Normal Thin Film	0.02 A/W	3 x 10^{10} Jones
$MAPbI_3$ Crystals on substrates	20 A/W	1.48 x 10^{13} Jones

Photodetector Device Model and Fluorescence

Lead halide perovskites ($MAPbI_3$) have large absorption cross section for photons having energies beyond 1.6 eV. The calculated penetration depth for an illumination of 450 nm (2.8 eV) is around 50 nm.[4] Due to small penetration depth of light at a wavelength of 450 nm, we excite excess energy hot electron hole pairs close to the surface of perovskite layers. Qualitatively in our model, the photocurrent is favored by the escape of charge carriers generated at the surface, to the corresponding electrodes upon applying a biasing voltage. According to the model of competing surface recombination and escape of charge carriers to the bulk crystal volume,[5–7] we expect that the high photocurrents we observe in large crystal devices are accompanied by relatively low photoluminescence by and large originating from the surface. In the case of a normal polycrystalline thin film device, the excess recombination at the surface leads to very low photocurrent and poor photodetector characteristics.

Such a behavior is reflected in the power dependence of photoluminescence intensity as shown in Figure S16. The peak intensity of the photoluminescence emitted from the crystals and from the thin film differ by a factor of approximately 30.

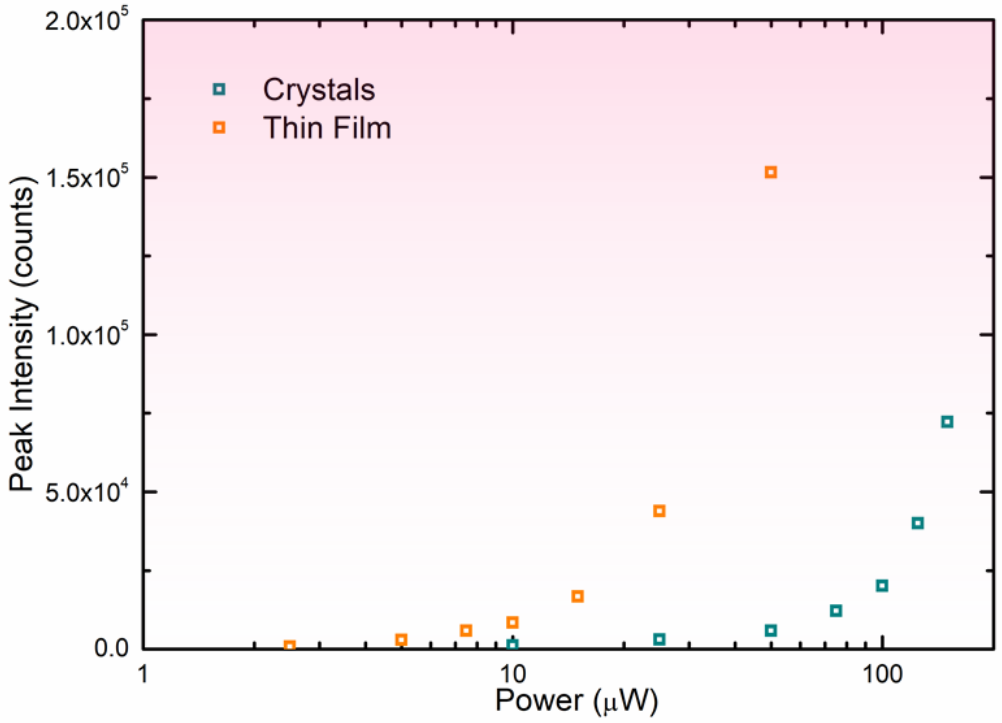

Figure S17: Dependence of the photoluminescence peak intensity on excitation power (λ_{exc} = 450 nm)

A quantitative correlation between photoluminescence intensity of crystals and polycrystalline thin films as well as their photocurrent dependences on crystal sizes is now ongoing.

Table S3: Performance comparison of various $MAPbI_3$ photoconductors from literatures.

Device architecture	Light (nm)	Responsivity (AW^{-1})	Detectivity (Jones)	On/off ratio	Rise-time/ Fall-time (ms)	Device Electric Field ($V\mu m^{-1}$)	Ref.
FTO/$MAPbI_3$/FTO	445	20	1.48×10^{13}	1.4×10^3	0.75/1.75	0.08	This work
ITO/$MAPbI_3$/ITO	830	275	10^{13}	-	0.03/0.02	1	[8]
Au/$MAPbI_3$/Au	420	13.6	5.25×10^{12}	-	0.08/0.24	0.1	[9]
Au/$MAPbI_3$/Au	650	0.1	1.02×10^{12}	3.4×10^2	0.3/0.4	0.025	[10]
Pt/$MAPbI_3$/Pt	400-700	<0.1	1.3×10^{11}	10^4	90/20	0.2	[11]
ITO/$MAPbI_3$/Au	White light	0.03	10^{10}	-	20.47/13.81	0.15	[12]
Au/$MAPbI_3$/Au	700	10.33	-	10^5	0.020/0.010	0.2	[13]
ITO/$MAPbI_3$/ITO	365	3.49	-	-	200/<200	0.2	[14]
Au/$MAPbI_3$/Au*	532	953	-	224	0.07/0.06	0.05	[15]
Au/$MAPbI_3$/Au	White light	7.92	-	130	<200/<200	0.06	[16]
ITO/$MAPbI_3$/ITO	White light	0.02-0.16	-	-	2200/300	<1	[17]

*Single crystal device

REFERENCES

(1) Shi, D.; Adinolfi, V.; Comin, R.; Yuan, M.; Alarousu, E.; Buin, A.; Chen, Y.; Hoogland, S.; Rothenberger, A.; Katsiev, K.; et al. Low Trap-State Density and Long Carrier Diffusion in Organolead Trihalide Perovskite Single Crystals. *Science (80-.).* **2015**, *347* (6221), 519–522. https://doi.org/10.1126/science.aaa2725.

(2) Jeon, N. J.; Noh, J. H.; Kim, Y. C.; Yang, W. S.; Ryu, S.; Seok, S. Il. Solvent Engineering for High-Performance Inorganic–Organic Hybrid Perovskite Solar Cells. *Nat. Mater.* **2014**, *13* (9), 897–903. https://doi.org/10.1038/nmat4014.

(3) Wu, T.; Ahmadi, M.; Hu, B. Giant Current Amplification Induced by Ion Migration in Perovskite Single Crystal Photodetectors. *J. Mater. Chem. C* **2018**, *6* (30), 8042–8050. https://doi.org/10.1039/c8tc02334d.

(4) Yang, Y.; Yang, M.; Moore, D. T.; Yan, Y.; Miller, E. M.; Zhu, K.; Beard, M. C. Top and Bottom Surfaces Limit Carrier Lifetime in Lead Iodide Perovskite Films. *Nat. Energy* **2017**, *2* (2), 16207. https://doi.org/10.1038/nenergy.2016.207.

(5) Yamada, Y.; Yamada, T.; Phuong, L. Q.; Maruyama, N.; Nishimura, H.; Wakamiya, A.; Murata, Y.; Kanemitsu, Y. Dynamic Optical Properties of CH<inf>3</Inf>NH<inf>3</Inf>PbI<inf>3</Inf> Single Crystals As Revealed by One- and Two-Photon Excited Photoluminescence Measurements. *J. Am. Chem. Soc.* **2015**, *137* (33), 10456–10459. https://doi.org/10.1021/jacs.5b04503.

(6) Alsari, M.; Szumilo, M.; Vru ini , M.; Beeson, H. J.; Friend, R. H.; Richter, J. M.; Lamboll, R.; Crespo-Quesada, M.; Ehrler, B.; Pazos-Outon, L. M.; et al. Photon Recycling in Lead

Iodide Perovskite Solar Cells. *Science (80-.).* **2016**, *351* (6280), 1430–1433. https://doi.org/10.1126/science.aaf1168.

(7) Ding, J.; Lian, Z.; Li, Y.; Wang, S.; Yan, Q. The Role of Surface Defects in Photoluminescence and Decay Dynamics of High-Quality Perovskite MAPbI3Single Crystals. *J. Phys. Chem. Lett.* **2018**, *9* (15), 4221–4226. https://doi.org/10.1021/acs.jpclett.8b01898.

(8) Saidaminov, M. I.; Haque, M. A.; Savoie, M.; Abdelhady, A. L.; Cho, N.; Dursun, I.; Buttner, U.; Alarousu, E.; Wu, T.; Bakr, O. M. Perovskite Photodetectors Operating in Both Narrowband and Broadband Regimes. *Adv. Mater.* **2016**, 8144–8149. https://doi.org/10.1002/adma.201601235.

(9) Deng, W.; Zhang, X.; Huang, L.; Xu, X.; Wang, L.; Wang, J.; Shang, Q.; Lee, S. T.; Jie, J. Aligned Single-Crystalline Perovskite Microwire Arrays for High-Performance Flexible Image Sensors with Long-Term Stability. *Adv. Mater.* **2016**, *28* (11), 2201–2208. https://doi.org/10.1002/adma.201505126.

(10) Deng, H.; Yang, X.; Dong, D.; Li, B.; Yang, D.; Yuan, S.; Qiao, K.; Cheng, Y. B.; Tang, J.; Song, H. Flexible and Semitransparent Organolead Triiodide Perovskite Network Photodetector Arrays with High Stability. *Nano Lett.* **2015**, *15* (12), 7963–7969. https://doi.org/10.1021/acs.nanolett.5b03061.

(11) Kwon, K. C.; Hong, K.; Van Le, Q.; Lee, S. Y.; Choi, J.; Kim, K. B.; Kim, S. Y.; Jang, H. W. Inhibition of Ion Migration for Reliable Operation of Organolead Halide Perovskite-Based Metal/Semiconductor/Metal Broadband Photodetectors. *Adv. Funct. Mater.* **2016**, *26* (23), 4213–4222. https://doi.org/10.1002/adfm.201600405.

(12) Gu, L.; Tavakoli, M. M.; Zhang, D.; Zhang, Q.; Waleed, A.; Xiao, Y.; Tsui, K. H.; Lin, Y.; Liao, L.; Wang, J.; et al. 3D Arrays of 1024-Pixel Image Sensors Based on Lead Halide Perovskite Nanowires. *Adv. Mater.* **2016**, *28* (44), 9713–9721. https://doi.org/10.1002/adma.201601603.

(13) Wang, W.; Ma, Y.; Qi, L. High-Performance Photodetectors Based on Organometal Halide Perovskite Nanonets. *Adv. Funct. Mater.* **2017**, *27* (12). https://doi.org/10.1002/adfm.201603653.

(14) Hu, X.; Zhang, X.; Liang, L.; Bao, J.; Li, S.; Yang, W.; Xie, Y. High-Performance Flexible Broadband Photodetector Based on Organolead Halide Perovskite. *Adv. Funct. Mater.* **2014**, *24* (46), 7373–7380. https://doi.org/10.1002/adfm.201402020.

(15) Lian, Z.; Yan, Q.; Lv, Q.; Wang, Y.; Liu, L.; Zhang, L.; Pan, S.; Li, Q.; Wang, L.; Sun, J.-L. High-Performance Planar-Type Photodetector on (100) Facet of MAPbI 3 Single Crystal. *Sci. Rep.* **2015**, *5* (1), 16563. https://doi.org/10.1038/srep16563.

(16) Fang, H.; Li, Q.; Ding, J.; Li, N.; Tian, H.; Zhang, L.; Ren, T.; Dai, J.; Wang, L.; Yan, Q. A Self-Powered Organolead Halide Perovskite Single Crystal Photodetector Driven by a DVD-Based Triboelectric Nanogenerator. *J. Mater. Chem. C* **2016**, *4* (3), 630–636. https://doi.org/10.1039/C5TC03342J.

(17) Lu, H.; Tian, W.; Cao, F.; Ma, Y.; Gu, B.; Li, L. A Self-Powered and Stable All-Perovskite Photodetector-Solar Cell Nanosystem. *Adv. Funct. Mater.* **2016**, *26* (8), 1296–1302. https://doi.org/10.1002/adfm.201504477.